Frustration-driven C_4 symmetric order in a naturally-heterostructured superconductor Sr_2VO_3FeAs

Jong Mok Ok[1,2], S.-H. Baek [3], C. Hoch[4], R.K. Kremer[4], S.Y. Park [5], Sungdae Ji[1,5], B. Büchner[3], J.-H. Park[1,5,6], S.I. Hyun[7], J.H. Shim[7], Yunkyu Bang[8], E.G. Moon[9], I.I. Mazin[10] & Jun Sung Kim[1,2]

A subtle balance between competing interactions in iron-based superconductors (FeSCs) can be tipped by additional interfacial interactions in a heterostructure, often inducing exotic phases with unprecedented properties. Particularly when the proximity-coupled layer is magnetically active, rich phase diagrams are expected in FeSCs, but this has not been explored yet. Here, using high-accuracy ^{75}As and ^{51}V nuclear magnetic resonance measurements, we investigate an electronic phase that emerges in the FeAs layer below $T_0 \sim 155\,K$ of Sr_2VO_3FeAs, a naturally assembled heterostructure of an FeSC and a Mott-insulating vanadium oxide. We find that frustration of the otherwise dominant Fe stripe and V Neel fluctuations via interfacial coupling induces a charge/orbital order in the FeAs layers, without either static magnetism or broken C_4 symmetry, while suppressing the Neel antiferromagnetism in the $SrVO_3$ layers. These findings demonstrate that the magnetic proximity coupling stabilizes a hidden order in FeSCs, which may also apply to other strongly correlated heterostructures.

[1] Department of Physics, Pohang University of Science and Technology, Pohang 790-784, Korea. [2] Center for Artificial Low Dimensional Electronic Systems Institute for Basic Science, Pohang 790-784, Korea. [3] IFW Dresden, Helmholtzstr. 20, 01069 Dresden, Germany. [4] Max-Planck-Institut für Festkörperforschung, Heisenbergstraβe 1, D-70569 Stuttgart, Germany. [5] Max Planck POSTECH Center for Complex Phase Materials Pohang University of Science and Technology, Pohang 790-784, Korea. [6] Division of Advanced Materials Science Pohang University of Science and Technology, Pohang 790-784, Korea. [7] Department of Chemistry, Pohang University of Science and Technology, Pohang 790-784, Korea. [8] Department of Physics, Chonnam National University, Gwangju 500-757, Korea. [9] Department of Physics, Korea Advanced Institute of Science and Technology, Daejeon 305-701, Korea. [10] Naval Research Laboratory code 6390, 4555 Overlook Avenue S.W., Washington, DC 20375, USA. Correspondence and requests for materials should be addressed to S.-H.B. (email: sbaek.fu@gmail.com) or to J.S.K. (email: js.kim@postech.ac.kr)

In strongly correlated electron materials, including cuprates, transition metal oxides (TMOs), and iron-based superconductors (FeSCs), competing interactions of spin, charge, and orbital degrees of freedom lead to complex and rich phase diagrams, extremely sensitive to external perturbations. Especially impressive is the modification of the phase diagram via introducing interfacial interactions, as intensively studied for the heterostructures of high-T_c cuprates[1–5] or TMOs[6,7], showing the enhanced T_c or emergent phases that cannot be stabilized in their constituent layer alone. The similar effect has also been found in FeSCs, for example, in FeSe monolayers on top of nonmagnetic SrTiO₃[8–10] showing drastically enhanced T_c, arguably higher than 100 K. Although the underlying mechanism is yet to be confirmed, the interfacial coupling is considered to be critical and may further enhance T_c in the superlattice[11]. Of particular interest is when the proximity-coupled layer is strongly correlated and magnetically active. As found in heterostructures of high-T_c cuprates and magnetic TMOs[3–5], additional interfacial spin interaction, e.g., in proximity of a Mott insulator, may also induce distinct ground states in FeSCs[12], which however has not been explored so far.

Sr₂VO₃FeAs is an unusual naturally assembled superlattice of $[SrFeAs]^{+1}$ and $[SrVO_3]^{-1}$ layers[13]. Initially Sr₂VO₃FeAs was thought to have, because of the V bands, an unusual Fermi surface topology, incompatible with $s^{\pm}$ superconductivity scenario driven by spin fluctuation[14]. However, it was soon realized that the V $3d^2$ electrons in the SrVO₃ layer are strongly correlated and form a Mott-insulating state[15–17], while the partially filled Fe $3d^6$ state in the FeAs layer has considerable itinerancy and superconducts at $T_c \sim 35$ K[13,14,18]. These contrasting ground states in Sr₂VO₃FeAs make this system prototypical for strongly correlated heterostructures based on FeSCs and TMOs. Sr₂VO₃FeAs has the Fermi surface structure similar to that in other FeSCs[15,17], and thus is expected to show either the stripe antiferromagnetic (AFM) order with the wave vector $\mathbf{Q} = (\pi, 0)$, or the corresponding nematic phase, or enhanced spin fluctuations at low temperature with the same wave vector[19]. There is in fact a second-order transition observed at $T_0 \sim 155$ K with a sizable entropy loss of $\sim 0.2R\ln 2$ (R is the gas constant)[20–22]. With no evidence of a static magnetic order or another apparent symmetry breaking, the hidden nature of this phase transition, similar to the famous hidden order in underdoped cuprates or a heavy fermion system URu₂Si₂, remains elusive and controversial[20–26], posing a challenge to our understanding of the physics of FeSCs in proximity of a Mott insulator.

Here we report that an emergent electronic phase is developed below $T_0 = 155$ K in Sr₂VO₃FeAs, which is highly distinct in nature from the transitions found in other FeSCs. Using high-accuracy ⁷⁵As and ⁵¹V nuclear magnetic resonance (NMR) measurements on single crystals under various field orientations, we unambiguously show that the transition occurs in the FeAs layer, not the SrVO₃ layer, without breaking either time reversal symmetry or the underlying tetragonal lattice symmetry. This implies that the typical stripe AFM and C_2 nematic phases in the FeAs layers as well as the Neel antiferromagnetism in the SrVO₃ layer are significantly suppressed by the interfacial coupling between itinerant iron electrons and localized vanadium spins. We propose that the observed phase is a C_4-symmetric charge/orbital order, which to our knowledge has never been observed in iron or vanadium-based materials, triggered by frustration of the otherwise dominant Fe stripe and V Neel fluctuations. Such a strong modification of the ground state is not common in other strongly correlated TMO heterostructures[3–5], which highlights that FeSCs, itinerant systems with complex interplay of spin/charge/orbital degrees of freedom, have competing ground states related to the Fermi surface instabilities, and thus are extremely sensitive to additional interfacial interactions in heterostructures.

Results

Transport and magnetic properties. Our transport and magnetic measurements on single crystalline Sr₂VO₃FeAs shown in Fig. 1b, c confirm that the transition at T_0 is intrinsic. A weak, but discernible, anomaly is observed at $T_0 \sim 155$ K in the resistivity (ρ), even more pronounced in its temperature derivative dρ/dT. The magnetic susceptibility $\chi(T)$ also shows an anomaly at T_0. Above T_0, $\chi(T)$ is several times larger than in typical FeSCs and follows the Curie–Weiss law with a Curie–Weiss temperature $T_{CW} \sim -100$ K (see Supplementary Note 2). The effective magnetic moment is consistent with $S = 1$ expected for the V^{3+} ions (Fig. 1a), suggesting that $\chi(T)$ is dominated by localized V spins. At $T_0 \sim 155$ K, $\chi(T)$ for both $H \parallel ab$ and $H \parallel c$ exhibits a small jump, which corresponds to a magnetization of $\sim 10^{-3}$ μ_B/f.u., three orders of magnitude smaller than typical values of V^{3+} ions (~ 1.8 μ_B) in vanadium oxides[16] and Fe ions (~ 0.8 μ_B) in FeSCs[27]. Such weak anomalies in $\rho(T)$ and $\chi(T)$, in contrast to a strong one in the specific heat[20–22], question the previous conjectures of a long-range ordering of either V or Fe spins[20–26], and suggest that this weak ferromagnetic response is only a side effect of the true transition. However, another anomaly at $T_N \sim 45$ K in both $\chi_{ab}(T)$ and $\chi_c(T)$ turns out to reflect a long-range ordering of Fe, but still not V spins, as discussed below. Notably, neither transition is consistent with the typical stripe AFM or nematic orders for FeSCs.

⁷⁵As and ⁵¹V NMR spectroscopy. To gain further insight into the transition at T_0 on a microscopic level, we measured NMR on ⁷⁵As and ⁵¹V nuclei as a function of temperature for field orientations parallel to a (100), c (001), and the (110) directions (Fig. 2 and the Supplementary Fig. 4). The ⁵¹V probes the V spin order directly and the ⁷⁵As is a proxy for the Fe sites, which allows us to probe the two magnetic ions separately. A dramatic change of the ⁷⁵As line occurs near $T_0 \sim 155$ K as shown in Fig. 2a, consistent with the anomalies in $\rho(T)$ and $\chi(T)$. Near 180 K, the ⁷⁵As signal starts to lose its intensity rapidly and is not detectable between 150 and 170 K due to the shortening of the spin–spin relaxation time T_2 (ref. [26]). Strikingly, the signal recovers below ~ 150 K at substantially higher frequencies, in a similar fashion for both field orientations. We emphasize that these behaviors of ⁷⁵As NMR have never been observed so far in other FeSCs as clearly shown in Supplementary Fig. 5. This is better shown in terms of the Knight shift $^{75}\mathcal{K} \equiv (f - \nu_0)/\nu_0$, where $\nu_0 \equiv \gamma_n H$ with the nuclear gyromagnetic ratio γ_n (see Fig. 2c). $^{75}\mathcal{K}$ changes abruptly at $T_0 \sim 155$ K without any peak splitting or broadening of the full-width at half-maximum (FWHM) across T_0. Conversely, the ⁵¹V line barely shifts below T_0 and down to 20 K (Fig. 2b, d), while its FWHM gradually increases below T_0. The nearly unchanged ⁵¹V NMR line signals that the V spins remain disordered down to low temperatures. This contrasting behavior of the ⁷⁵As and ⁵¹V spectra unambiguously proves that the transition at T_0 occurs in the FeAs layer and not in the SrVO₃ layer, contrary to previous claims[20–25].

Having established that the phase transition at T_0 occurs in the FeAs layer, we examined the low-energy Fe spin dynamics, as probed by the ⁷⁵As spin–lattice relaxation rate T_1^{-1}, which reflects local spin fluctuations. As shown in Fig. 3, at $T \gtrsim 240$ K, $(T_1 T)^{-1}$ exhibits a typical Curie–Weiss-like behavior with an anisotropy $T_{1,a}^{-1}/T_{1,c}^{-1} \approx 1.5$. This is expected for a directionally disordered state with local stripe AFM correlations with $\mathbf{Q} = (\pi, 0)$ and has been observed in many FeSCs[28,29] (see Supplementary Note 6). With lowering temperature, a critical slowdown of the $(\pi, 0)$ spin fluctuations usually condenses into the C_2 stripe AFM phase. For Sr₂VO₃FeAs, however, this critical growth is arrested at $T \sim 200$ K, showing a broad peak of $(T_1 T)^{-1}$ with an unusually large
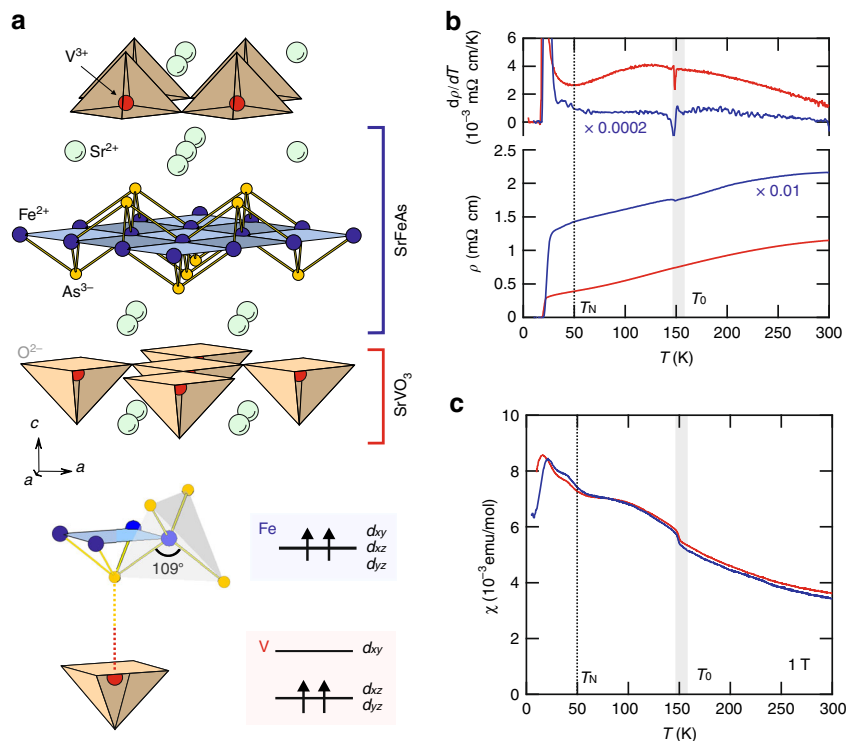
Fig. 1 Basic properties of Sr_2VO_3FeAs. **a** The crystal structure of Sr_2VO_3FeAs as a naturally assembled heterostructure of the $[SrFeAs]^{+1}$ and $[SrVO_3]^{-1}$ layers. V ions form a network of corner-sharing tetrahedra, while FeAs layers consist of edge-sharing $FeAs_4$ tetrahedra as in other iron-based superconductors. The local structure of an $FeAs_4$ tetrahedron and a VO_3 pyramid is highlighted at the bottom. $FeAs_4$ tetrahedra provide a moderate cubic crystal field splitting, much smaller than the band widths, while the VO_3 unit is missing one O entirely, and thus develops a strong Jahn–Teller splitting. The d_{xy} orbital is pushed up, and the two V d electrons occupy the d_{xz} and d_{yz} states, forming an $S = 1$ spin. The Fe and V planes are bridged by the As atoms, as indicated by the dashed line. **b** The resistivity $\rho(T)$ in the ab plane (red) and along the c axis (blue) shows a weak anomaly at $T_0 \sim 155$ K (blue highlighted region), which is more clear in their temperature derivatives (top panel). The large c-axis resistivity, which was scaled down by a factor of 100, is consistent with the quasi-2D nature of the material. **c** The magnetic susceptibility $\chi(T)$, taken at $H = 1$ T for $H \perp c$ and $H \parallel c$, shows clear anomalies at T_0 and also at $T_N \sim 45$ K
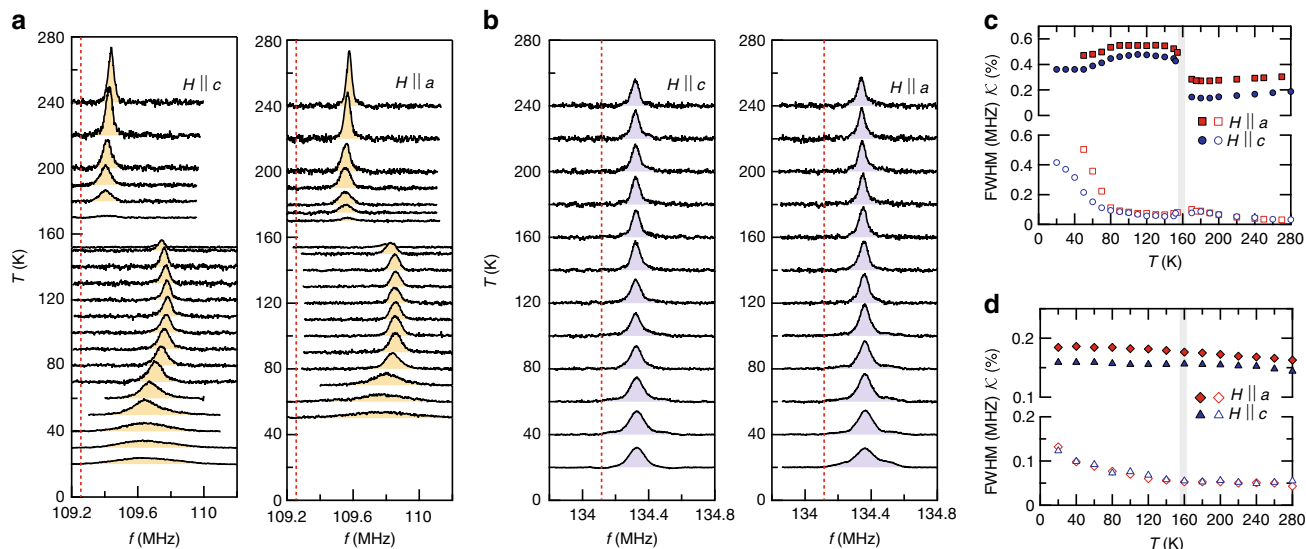

Fig. 2 NMR spectra and their analysis for the Sr_2VO_3FeAs single crystal. ^{75}As (**a**) and ^{51}V (**b**) NMR spectra as a function of temperature, measured at $H = 15$ and 12 T, respectively, for the fields oriented along the a and c axes. The unshifted Larmor frequency ($\nu_0 \equiv \gamma_n H$) is marked by the red vertical lines. While the ^{51}V spectrum is nearly temperature independent down to 20 K, the ^{75}As spectra in both field directions show a sudden shift at $T_0 \sim 155$ K. **c**, **d** Temperature dependences of the ^{75}As and ^{51}V spectra in terms of the Knight shift ($\mathcal{K}$) and the full-width at half-maximum (FWHM), respectively. Below T_0, a nearly isotropic large jump of the ^{75}As Knight shift takes place without any magnetic line broadening, contrasting with the ^{51}V spectra that remain unchanged
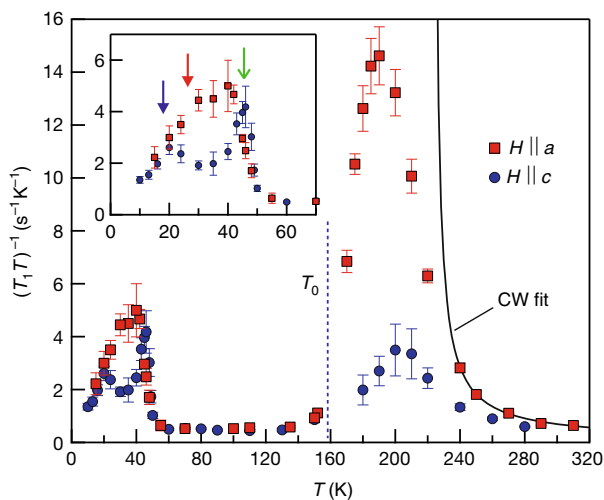
Fig. 3 Fe spin fluctuations. Temperature dependence of the ^{75}As spin–lattice relaxation rate divided by temperature $(T_1 T)^{-1}$ measured at 15 T. The error bars reflect the uncertainty in the fitting procedure. At high temperatures, $(T_1 T)^{-1}$ is well described by a Curie–Weiss (CW) law (solid line). Below ~240 K, it deviates from the diverging behavior and drops at lower temperatures, forming a large peak centered at ~190 K. At low temperatures below 120 K, $(T_1 T)^{-1}$ reaches a constant value comparable to that observed at the high temperature limit, implying that the spin fluctuations are completely gapped out. $(T_1 T)^{-1}$ sharply turns up at ~50 K, indicating critical slowing down of spin fluctuations toward a magnetic order. In the inset, T_N ~ 45 K (green arrow) was identified from the sharp peak observed for $H \parallel c$. $(T_1 T)^{-1}$ drops at T_c, determined by the resistivity measurements under $H \parallel ab$ (red arrow) and $H \parallel c$ (blue arrow), microscopically probing bulk superconductivity in the magnetically ordered state

$T_{1,a}^{-1} / T_{1,c}^{-1} \approx 6$, and then the fluctuations harden all the way down to T_0. Across T_0, $(T_1 T)^{-1}$ barely changes and then quickly reaches a constant below T_0, behaving as a paramagnetic metal. This completely unexpected behavior in both $^{75}\mathcal{K}$ and $(T_1 T)^{-1}$ confirms that the transition at T_0 in Sr$_2$VO$_3$FeAs is unlike any transitions observed in FeSCs so far.

Let us now discuss possible orders established below T_0. First of all, we can eliminate the usual suspects: stripe, double-Q[30–33], and bicollinear[34] AFM orders, observed in other FeSCs. In the first case Q = $(\pi, 0)$ and the Fe spins aligned along the a axis ($s \parallel a$) generate a hyperfine field H_{hf} ~ 1.5 T along the c axis. This would be visible in the ^{75}As NMR spectra as a peak splitting of ~10 MHz for $H \parallel c$, which is far larger than the FWHM of our spectra (~0.05 MHz) and easily detectable. Similarly, for $s \parallel c$, an ^{75}As peak splitting is expected for $H \parallel a$. Even for $s \parallel b$, in which case no transferred H_{hf} and thus no peak splitting are expected, considerable line broadening due to the directional fluctuations of Fe spins should be seen in experiments. Neither splitting nor broadening is observed in our experiments (Fig. 2a). For the double-Q AFM state[30–33], a combination of two spin density waves with Q = $(\pi, 0)$ and $(0, \pi)$, the magnetization vanishes at one of the two Fe sublattices and is staggered in the other. Thus, the ^{75}As peak splitting is expected for either $H \parallel c$ ($s \parallel a$) or $H \parallel a$ ($s \parallel c$), as discussed in the Supplementary Note 5, which can be ruled out by experiments. The bicollinear AFM order[34] can also be excluded with even more confidence. In this case, the As environment is spin-imbalanced (three neighboring Fe spins are aligned in one direction, and the fourth one in the opposite), and already a plain exchange coupling would generate two inequivalent As sites and thus a measurable splitting for any direction of external fields. Similarly, other AFM orders with more

complicated spin structures, such as a plaquette AFM order, are excluded as discussed in the Supplementary Note 5. This conclusion is further supported by the absence of the diverging behavior in $(T_1 T)^{-1}$ across T_0 (Fig. 3).

Having excluded static magnetic order, we consider now nematic or, as it is occasionally called, vestigial partners of various AFM orders. The only nematic order observed so far in FeSCs is the stripe-nematic order that creates an imbalance in the orbital population between Fe d_{xz} and d_{yz} states (Fig. 4b). This, in turn, induces an imbalance between As p_x and p_y orbitals and dipolar in-plane anisotropy of the As Knight shift in the twinned crystals, as observed in e.g., LaFeAsO for $H \parallel a$ below the nematic transition temperature[29]. A similar behavior is expected for the nematic partner of the bicollinear order (Fig. 4c), which breaks the C_4 symmetry such that the (110) and (1$\bar{1}$0) directions are not equivalent[35,36]. If the generated imbalance between the corresponding orbital Fe-$d_{xz} \pm d_{yz}$ is of the same order as in the stripe-nematic case, a peak splitting for $H \parallel$ (110) should be detected. And, for the nematic partner of the plaquette magnetic order, two inequivalent sites and thus a sizable splitting are expected for every field direction. Yet, none of these signatures appear in our ^{75}As spectra for $H \parallel a$ (100), c (001), and (110) directions (Fig. 2a, b and the Supplementary Fig. 4). Furthermore, our single-crystal X-ray diffraction (XRD) (see Supplementary Note 1) as well as the recent ARPES study[17] do not reveal any signature of a C_4 symmetry breaking.

Since the transition at T_0 retains the C_4 symmetry, and in the absence of a long-range magnetic order, this transition must generate a change in the relative occupations of the C_4 orbitals, namely d_{xy}, d_{z^2}, $d_{x^2-y^2}$, and $d_{xz} \pm i d_{yz}$. Given that at high temperature we see clear indications of strong spin fluctuations, we looked for a spin-driven scenario conserving the C_4 symmetry; a good candidate is the vestigial (nematic) partner of the double-Q AFM order[37]. It can be visualized (Fig. 4d) as a superposition of two charge/orbital density waves with Q = $(\pi, 0)$ and $(0, \pi)$, which preserves the C_4 symmetry without unit-cell doubling. This phase has a broken translational symmetry in the Fe-only square lattice, but not in the unit cell doubled to include the As atoms[37]. Formation of the intra-unit-cell charge/orbital density wave affects the Fe–As hybridization and modifies the hyperfine coupling via isotropic Fermi-contact and core-polarization interactions, accounting for the nearly isotropic $^{75}\mathcal{K}$ Knight shift (Fig. 2). One may note that due to dipole or orbital hyperfine interactions, the Knight shift can split for a field parallel to (110), because half of the As sites have paramagnetic neighbors along (110), and half along (1$\bar{1}$0). However, the difference in the d orbital occupations between nonmagnetic and paramagnetic Fe are expected to be small, likely a few percent (see Supplementary Note 5), in which case the splitting will be below detection, consistent with our experiments.

If we assume a nonmagnetic origin, another plausible candidate could be an orbital-selective Mott transition. In this case, the most correlated Fe orbital state, likely d_{xy}, experiences a Mott–Hubbard transition, becoming essentially gapped, while the other orbitals remain itinerant. The resulting occupation change in the d_{xy} state of all Fe sites (Fig. 4e) uniformly changes the hyperfine field at the As sites, retaining the C_4 symmetry and explaining the nearly isotropic change of $^{75}\mathcal{K}$ (Fig. 2). Indeed a possibility of such transition has been discussed, but, admittedly, not in undoped pnictides, but in more strongly correlated chalcogenides[38] and (strongly underdoped) KFe$_2$As$_2$[39,40]. We note that as compared to the orbital-selective Mott phase, the former vestigial double-Q phase breaks the additional translational symmetry, which may allow experimental distinction by neutron scattering when bigger crystals become available.
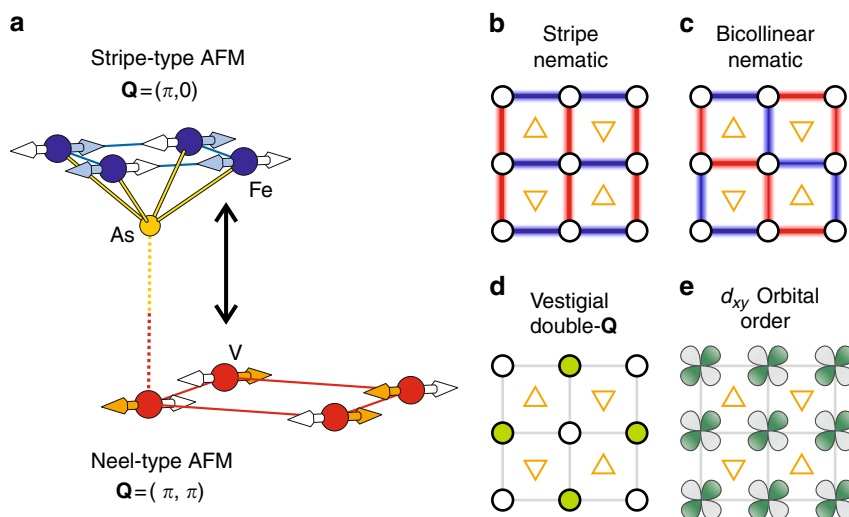
Fig. 4 Possible orders retaining a C_4 symmetry without long-range magnetism. **a** Stripe-type and Neel-type AFM fluctuations of Fe and V spins, respectively, at high temperatures. Two arrows at each Fe and V sites illustrate fluctuating moments with their own spin correlation, indicated by different colors. These different types of AFM fluctuations are frustrated via Fe–V spin coupling (vertical arrow) developed at low temperatures. **b–d** Various vestigial ordered phases resulting from melting the corresponding magnetic orders: the typical stripe nematic (x/y symmetry broken), the bicollinear nematic ((x + y)/(x − y) and the translation symmetry broken)[36], and the vestigial double-**Q** phase (only the translational symmetry broken)[37]. **e** d_{xy} orbital order driven by a possible orbital-selective Mott transition. As opposed to **b–d**, there is no symmetry breaking at all in this phase compared to the high-temperature phase. In **b** and **c**, the symmetry breaks because some bonds are predominantly ferromagnetic (red) and some predominantly antiferromagnetic (blue). In **d**, green circles indicate completely nonmagnetic Fe sites, while open circles correspond to fluctuation paramagnetic sites. The As sites above (up-triangle) and below (down-triangle) the Fe plane are also shown. Note that only **d** and **e** are consistent with the observed C_4 symmetry, as discussed in the main text, and are our favorite candidates for the hidden order below T_0

As mentioned, Sr_2VO_3FeAs experiences another transition at $T_N \approx 45$ K, which can be identified as a spin density wave highly distinct from the typical stripe AFM. Indeed, $(T_1T)^{-1}$ climbs sharply below 60 K ($\ll T_0$) for both $H \parallel a$ and $H \parallel c$, indicating a critical slow-down of spin fluctuations toward a magnetic ordering at $T_N \sim 45$ K. However, $T_{1,a}^{-1}/T_{1,c}^{-1}$ remains isotropic, suggesting that the coupling between Fe spins and As is due to hybridization, which can only generate a magnetic moment on As if As environment is spin-imbalanced. This excludes such AFM orders as stripe, Neel, or double-**Q**, but would be consistent with a longer period AFM order. Also the progressive broadening of ^{75}As spectrum at low temperatures, as shown in Fig. 2a, c, suggests a long wavelength, and possibly incommensurate, spin density wave. Neutron diffraction[23,24], which observed magnetic Bragg peaks at **Q** = (1/8, 1/8, 0) below $T_N \sim 45$ K, is consistent with this conclusion, although it was incorrectly attributed to an ordering of V spins in the previous studies[16,20–25]. Upon further temperature lowering, $(T_1T)^{-1}$ abruptly drops at T_c. This proves that the superconducting gap opens up on the magnetic Fe sites, and emerges on the background of the remaining, but still strong, spin fluctuations with a C_4 symmetry below T_N. How spin density wave competes or cooperates with superconductivity remains an important question.

Discussion

We shall now address an essential question: what suppresses the expected stripe order in the FeAs layer and the Neel order in the $SrVO_3$ layer? The former can be suppressed via the mechanism in which Neel-type spin fluctuations of the localized magnetic moments are coupled to the itinerant electrons' stripe spin fluctuation[12]. The stripe order, with **Q** = (π, 0) or (0, π), is relatively fragile and can give way to bicollinear, double-**Q**, and, possibly, plaquette orders, due to AFM fluctuation with additional **Q**'s[12,37,41]. Such magnetic frustration is due to the long-range

magnetic interactions, reflecting the itinerancy of Fe electrons. Fluctuation at **Q** = (π, π), normally weak in FeSCs, can be enhanced through coupling to the **Q** = (π, π) fluctuations of V spins[12] (Fig. 4a). This destabilizes the C_2 stripe AFM or nematic orders, but encourages the C_4 symmetric vestigial charge/orbital density wave phases[12,37]. Note that in $Sr_2(Mg,Ti)O_3FeAs$ and Ca_2AlO_3FeAs, isostructural compounds with nonmagnetic oxide layers, the standard stripe ordering is not suppressed[42,43]. Clearly additional Neel V spin fluctuations, frustrated with stripe Fe spin fluctuations via magnetic proximity coupling, are essential to stabilize an unusual hidden phase in Sr_2VO_3FeAs.

The coupling between the itinerant Fe electrons and the localized V spins also suppress the Neel order in the $SrVO_3$ layer. In the $SrVO_3$ layers, the nearest neighbor superexchange interaction would dominate and generate a stable Neel order. In fact, compared to other V^{3+} perovskite oxides, such as $LaVO_3$, $SrVO_3FeAs$ should have stronger exchange coupling, because of the straighter V–O–V bonds. However, the measured Curie–Weiss temperature of $T_{CW} \sim -100$ K in Sr_2VO_3FeAs is considerably lower than $T_{CW} \sim -700$ K in $LaVO_3$[44]. The unexpectedly low T_{CW} comes from an additional ferromagnetic coupling between the V spins via indirect double-exchange-like interaction mediated by the Fe electrons[45]. This frustrates and weakens the V AFM super-exchange interaction suppressing the long-range V spin order at low temperatures. Indeed, in our detailed LDA + U calculations, we found that the calculated magnetic interaction is extremely sensitive to the on-site Coulomb energy U and the Hund's coupling J (note that these corrections were only applied to V, and not to Fe orbitals). At $U - J = 5$ eV, the superexchange interaction, which is inversely proportional to U, is significantly suppressed, while the Fe-mediated one is enhanced, so that the net magnetic interaction becomes weakly ferromagnetic in the planes. For $U - J = 4$, it changes sign and becomes antiferromagnetic, consistent with a previous report[16]. This demonstrates that the

$SrVO_3$ lies on the borderline of competing phases due to a delicate balance between the superexchange and the additional indirect interactions. At the same time, coupling between the stripe fluctuations in the Fe plane at $\mathbf{Q} = (\pi, 0)$ and Neel fluctuations in the V plane $\mathbf{Q} = (\pi, \pi)$ suppresses both orders even further[12] and prevents V spins form ordering. The interfacial Fe–V interaction is again crucial for the Mott-insulating $SrVO_3$ layers to remain in a nearly paramagnetic ground state. Our findings therefore manifest that the physics of FeSCs can become even richer in the proximity of other correlated systems and also offer an avenue for exploring unusual ground state in the correlated heterostructures.

Methods

Crystal growth. Single crystals of Sr_2VO_3FeAs were grown using self-flux techniques as follows. The mixture of SrO, VO_3, Fe, SrAs, and FeAs powders with a stoichiometry of Sr_2VO_3FeAs:FeAs = 1:2 were pressed into a pellet and sealed in an evacuated quartz tube under Ar atmosphere. The samples were heated to 1180 °C, held at this temperature for 80 h, cooled slowly first to 950 °C at a rate of 2 °C/h and then furnace-cooled. The plate-shaped single crystals were mechanically extracted from the flux. High crystallinity and stoichiometry are confirmed by the XRD and energy-dispersive spectroscopy. The typical size of the single crystals is $200 \times 200 \times 10\ \mu m^3$.

Single crystal characterization. Single-crystal XRD patterns were taken using an STOE single crystal diffractometer with image plate. Single crystal XRD reveals a good crystallinity in a tetragonal structure with $a = 3.9155(7)$ Å and $c = 15.608(4)$ Å, consistent with the previous studies on polycrystalline samples. Detailed information about single crystal XRD can be found in the Supplementary Information.

Conventional four-probe resistance of single crystals was measured in a 14 T Physical Property Measurement System. Single-crystal magnetizations were measured in a 5 T Magnetic Property Measurement System. The size of one crystal was too small (~0.15 mg) to measure the magnetization, thus 8 pieces of Sr_2VO_3FeAs single crystals (1.2 mg) were stacked together. All single crystals were carefully aligned along the c-axis or the ab-plane.

These measurements further confirm the quality of our single crystals. In heterostructured compounds, antisite mixing, here between Fe and V atoms, is known to be detrimental to maintain their intrinsic properties. The As NMR line width and the superconducting transition width are particularly sensitive to the antisite mixing. In our crystals, we found that the As NMR line width is ~30 kHz at 280 K, comparable with typical values of ~5–40 kHz found in other single crystalline FeSCs. Also that the V NMR line width of our single crystal is ~50 kHz at 280 K, much smaller than ~160 kHz, observed in polycrystalline sample[26]. Furthermore we also found that the superconducting transition in our Sr_2VO_3FeAs single crystal has a sharper resistive transition with a temperature width of $\Delta T_c \sim 3$ K, than found in polycrystalline Sr_2VO_3FeAs whose ΔT_c is typically larger than 5 K[13]. These observations consistently suggest that the antisite mixing, if any, cannot be sufficient to induce the observed unusual behavior in our Sr_2VO_3FeAs single crystal.

Nuclear magnetic resonance. ^{51}V (nuclear spin $I = 7/2$) NMR and ^{75}As ($I = 3/2$) NMR measurements were carried out at external magnetic fields of 14.983 and 11.982 T, respectively. The sample was rotated using a goniometer for the exact alignment along the external field. The NMR spectra were acquired by a standard spin–echo technique with a typical $\pi/2$ pulse length 2–3 μs and the spin–lattice relaxation rate was obtained by a saturation method.

Band structure calculations. Band structure calculations were performed using two standard codes: an all-electron linearized augmented plane wave method implemented in the WIEN2k package[46], and a pseudopotential VASP code[47]. In both cases the gradient-corrected functional of Perdew, Burke, and Ernzerhof was used, and special care was taken to ensure proper occupancy of V orbitals in the LDA + U calculations. LDA + U calculations are known to occasionally converge to metastable minima with incorrect orbital occupancy. Some calculations in the literature suffer from this problem. We ensured, by a proper selection of the starting configuration, that our calculations converge to the correct occupancy, and verified that by analyzing the calculated density of states for each independent run.

Data availability. All relevant data are available from the authors.

References

1. Gozar, A. et al. High-temperature interface superconductivity between metallic and insulating copper oxides. Nature 455, 782–785 (2008).
2. Wu, J. et al. Anomalous independence of interface superconductivity from carrier density. Nat. Mater. 12, 877–881 (2013).
3. Chakhalian, J. et al. Magnetism at the interface between ferromagnetic and superconducting oxides. Nat. Phys. 2, 244–248 (2006).
4. Satapathy, D. K. et al. Magnetic proximity effect in $YBa_2Cu_3O_7/La_{2/3}Ca_{1/3}MnO_3$ and $YBa_2Cu_3O_7/LaMnO_{3+\delta}$ superlattices. Phys. Rev. Lett. 108, 197201 (2012).
5. Driza, N. et al. Long-range transfer of electron-phonon coupling in oxide superlattices. Nat. Mater. 11, 675–681 (2012).
6. Hwang, H. Y. et al. Emergent phenomena at oxide interfaces. Nat. Mater. 11, 103–113 (2012).
7. Chakhalian, J., Freeland, J. W., Millis, A. J., Panagopoulos, C. & Rondinelli, J. M. Colloquium: emergent properties in plane view: strong correlations at oxide interfaces. Rev. Mod. Phys. 86, 1189–1202 (2014).
8. Tan, S. et al. Interface-induced superconductivity and strain-dependent spin density waves in FeSe/SrTiO3 thin films. Nat. Mater. 12, 634–640 (2013).
9. Ge, J.-F. et al. Superconductivity above 100 K in single-layer FeSe films on doped $SrTiO_3$. Nat. Mater. 14, 285–289 (2015).
10. Lee, J. J. et al. Interfacial mode coupling as the origin of the enhancement of T_c in FeSe films on SrTiO3. Nature 515, 245–248 (2014).
11. Coh, S., Lee, D.-H., Louie, S. G. & Cohen, M. L. Proposal for a bulk material based on a monolayer FeSe on SrTiO3 high-temperature superconductor. Phys. Rev. B 93, 245138 (2016).
12. Wang, X. & Fernandes, R. M. Impact of local-moment fluctuations on the magnetic degeneracy of iron-based superconductors. Phys. Rev. B 89, 144502 (2014).
13. Zhu, X. et al. Transition of stoichiometric Sr_2VO_3FeAs to a superconducting state at 37.2 K. Phys. Rev. B 79, 220512 (2009).
14. Lee, K.-W. & Pickett, W. E. Sr_2VO_3FeAs: a nanolayered bimetallic iron pnictide superconductor. Europhys. Lett. 89, 57008 (2010).
15. Qian, T. et al. Quasinested Fe orbitals versus Mott-insulating V orbitals in superconducting $Sr_2VfeAsO_3$ as seen from angle-resolved photoemission. Phys. Rev. B 83, 140513 (2011).
16. Nakamura, H. & Machida, M. Magnetic ordering in blocking layer and highly anisotropic electronic structure of high-T_c iron-based superconductor $Sr_2VfeAsO_3$: LDA + U study. Phys. Rev. B 82, 094503 (2010).
17. Kim, Y. K. et al. Possible role of bonding angle and orbital mixing in iron pnictide superconductivity: comparative electronic structure studies of LiFeAs and Sr_2VO_3FeAs. Phys. Rev. B 92, 041116 (2015).
18. Mazin, I. I. Sr_2VO_3FeAs as compared to other iron-based superconductors. Phys. Rev. B 81, 020507 (2010).
19. Johnston, D. C. The puzzle of high temperature superconductivity in layered iron pnictides and chalcogenides. Adv. Phys. 59, 803–1061 (2010).
20. Sefat, A. S. et al. Variation of physical properties in the nominal $Sr_4V_2O_6Fe_2As_2$. Physica C 471, 143–149 (2011).
21. Cao, G.-H. et al. Self-doping effect and successive magnetic transitions in superconducting $Sr_2VfeAsO_3$. Phys. Rev. B 82, 104518 (2010).
22. Tatematsu, S., Satomi, E., Kobayashi, Y. & Sato, M. Magnetic ordering in V-layers of the superconducting system of $Sr_2VFeAsO_3$. J. Phys. Soc. Jpn. 79, 123712 (2010).
23. Tegel, M. et al. Possible magnetic order and suppression of superconductivity by V doping in Sr_2VO_3FeAs. Phys. Rev. B 82, 140507 (2010).
24. Hummel, F., Su, Y., Senyshyn, A. & Johrendt, D. Weak magnetism and the Mott state of vanadium in superconducting Sr_2VO_3FeAs. Phys. Rev. B 88, 144517 (2013).
25. Munevar, J. et al. Static magnetic order of $Sr_4A_2O_6Fe_2As_2$ (A = Sc and V) revealed by Mössbauer and muon spin relaxation spectroscopies. Phys. Rev. B 84, 024527 (2011).
26. Ueshima, K. et al. Magnetism and superconductivity in $Sr_2VFeAsO_3$ revealed by ^{75}As- and ^{54}V-NMR under elevated pressures. Phys. Rev. B 89, 184506 (2014).
27. Huang, Q. et al. Neutron-diffraction measurements of magnetic order and a structural transition in the parent BaFe2As2 compound of FeAs-based high-temperature superconductors. Phys. Rev. Lett. 101, 257003 (2008).
28. Kitagawa, K., Katayama, N., Ohgushi, K., Yoshida, M. & Takigawa, M. Commensurate itinerant antiferromagnetism in BaFe2As2: ^{75}As-NMR studies on a self-flux grown single crystal. J. Phys. Soc. Jpn. 77, 114709 (2008).
29. Fu, M. et al. NMR search for the spin nematic state in a LaFeAsO single crystal. Phys. Rev. Lett. 109, 247001 (2012).
30. Avci, S. et al. Magnetically driven suppression of nematic order in an iron-based superconductor. Nat. Commun. 5, 3845 (2014).
31. Böhmer, A. E. et al. Superconductivity induced re-entrance of the orthorhombic distortion in $Ba_{1-x}K_xFe_2As_2$. Nat. Commun. 6, 7911 (2015).
32. Allred, J. M. et al. Double-Q spin-density wave in iron arsenide superconductors. Nat. Phys. 12, 493–498 (2016).

33. Waßer, F. et al. Spin reorientation in $Ba_{0.65}Na_{0.35}Fe_2As_2$ studied by single-crystal neutron diffraction. *Phys. Rev. B* **91**, 060505 (2015).

34. Ma, F., Ji, W., Hu, J., Lu, J.-Y. & Xiang, T. First-principles calculations of the electronic structure of tetragonal α-FeTe and α-FeSe crystals: evidence for a bicollinear antiferromagnetic order. *Phys. Rev. Lett.* **102**, 177003 (2009).

35. Bishop, C. B., Herbrych, J., Dagotto, E. & Moreo, A. Possible bicollinear nematic state with monoclinic lattice distortions in iron telluride compounds. *Phys. Rev. B* **96**, 035144 (2017).

36. Zhang, G., Glasbrenner, J. K., Flint, R., Mazin, I. I. & Fernandes, R. M. Double-stage nematic bond ordering above double stripe magnetism: application to $BaTi_2Sb_2O$. *Phys. Rev. B* **95**, 174402 (2017).

37. Fernandes, R. M., Kivelson, S. A. & Berg, E. Vestigial chiral and charge orders from bidirectional spin-density-waves: Application to the iron-based superconductors. *Phys. Rev. B* **93**, 014511 (2016).

38. Yu, R. & Si, Q. Orbital-selective Mott phase in multiorbital models for alkaline iron selenides $K_{1-x}Fe_{2-y}Se_2$. *Phys. Rev. Lett.* **110**, 146402 (2013).

39. Medici, L., Giovannetti, G. & Capone, M. Selective Mott physics as a key to iron superconductors. *Phys. Rev. Lett.* **112**, 177001 (2014).

40. Misawa, T., Nakamura, K. & Imada, M. Ab initio evidence for strong correlation associated with Mott proximity in iron-based superconductors. *Phys. Rev. Lett.* **108**, 177007 (2012).

41. Glasbrenner, J. K. et al. Effect of magnetic frustration on nematicity and superconductivity in iron chalcogenides. *Nat. Phys.* **11**, 953–958 (2015).

42. Yamamoto, K. et al. Antiferromagnetic order and superconductivity in $Sr_4(Mg_{0.5-x}Ti_{0.5+x})_2O_6Fe_2As_2$ with electron doping: ^{75}As-NMR Study. *J. Phys. Soc. Jpn.* **81**, 053702 (2012).

43. Kinouchi, H. et al. Antiferromagnetic spin fluctuations and unconventional nodeless superconductivity in an iron-based new superconductor ($Ca_4Al_2O_{6-y}$)(Fe_2As_2): ^{75}As nuclear quadrupole resonance study. *Phys. Rev. Lett.* **107**, 047002 (2011).

44. Mahajan, A. V., Johnston, D. C., Torgeson, D. R. & Borsa, F. Magnetic properties of $LaVO_3$. *Phys. Rev. B* **46**, 10966–10972 (1992).

45. Glasbrenner, J. K., Žutić, I. & Mazin, I. I. Theory of Mn-doped II-II-V semiconductors. *Phys. Rev. B* **90**, 140403 (2014).

46. Blaha, P., Schwarz, K., Madsen, G. K. H., Kvasnicka, D. & Luitz, J. *Wien2K: An Augmented Plane Wave + Local Orbitals Program for Calculating Crystal Properties* (Technische Universität Wien, Wien, 2001).

47. Kresse, G. & Furthmüller, J. Efficient iterative schemes for ab initio total-energy calculations using a plane-wave basis set. *Phys. Rev. B* **54**, 11169–11186 (1996).

Acknowledgements

Author contributions

Additional information

Supplementary Note 1. X-ray diffraction on Sr_2VO_3FeAs single crystals

Supplementary Fig. 1 shows X-ray diffraction patterns from a Sr_2VO_3FeAs single crystal at various (hkl) planes. The clear spots with no splitting confirm good crystallinity of the crystals without twin domains. The structure information determined from the single crystal XRD was listed in Supplementary Table 1. We note that the tetragonal crystal symmetry $(P4/nmm)$ describes well the observed Bragg reflections both at 297 K $(> T_0)$ and at 93 K $(< T_0)$. A refined crystal structure of Sr_2VO_3FeAs is shown in Supplementary Fig. 1n.
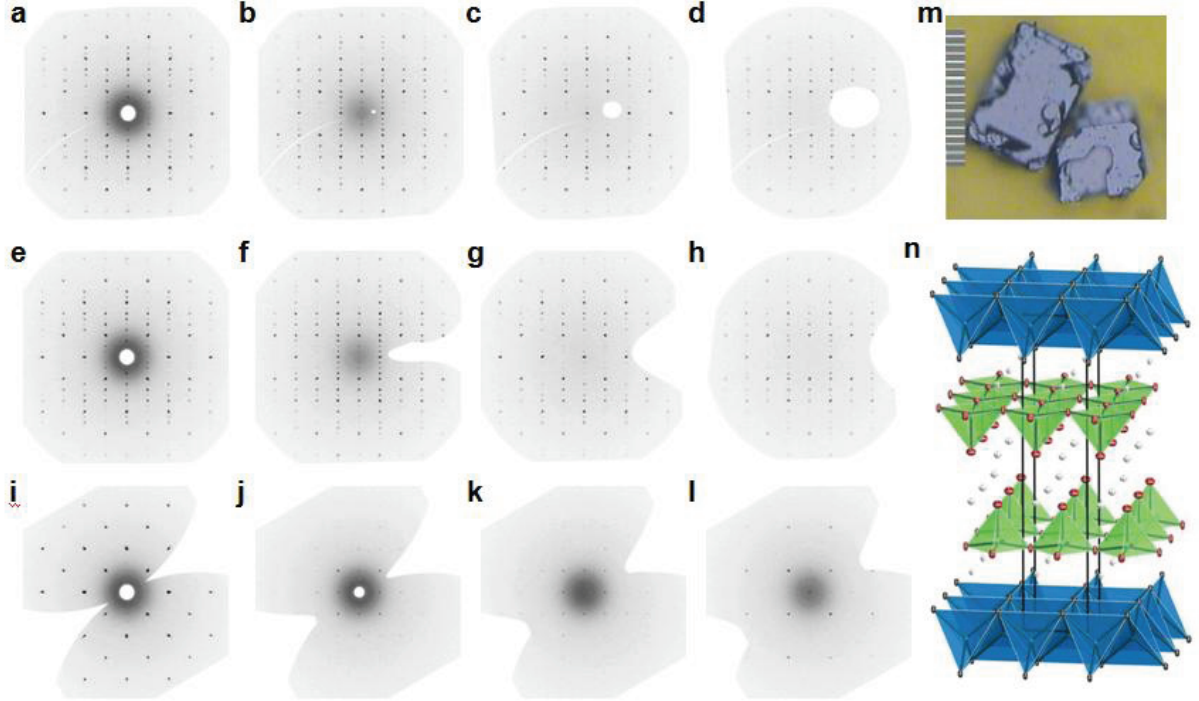
Supplementary Fig. 1: Single crystal X-ray diffraction patterns of Sr_2VO_3FeAs for **a** $(0kl)$ **b** $(1kl)$ **c** $(2kl)$ **d** $(3kl)$ **e** $(h0l)$ **f** $(h1l)$ **g** $(h2l)$ **h** $(h3l)$ **i** $(hk0)$ **j** $(hk1)$ **k** $(hk2)$ **l** $(hk3)$ planes. **m** A photograph of Sr_2VO_3FeAs single crystal grown by the self-flux method (scale bar size is 200μm). **n** Perspective view of the unit cell of Sr_2VO_3FeAs (light gray: Sr, blue: Fe, green: V, red: O, dark gray: As). All ellipsoids are drawn at a 90 % probability level. The square pyramids in green show the coordination of V(1) by four O(1) and one O(2), the blue tetrahedra depict the coordination of Fe(1) by four As(1). The c vector is vertical.

Supplementary Fig. 2a shows the single crystal X-ray diffractograms for two Bragg reflections at $(h\ k\ l) = (0\ 0\ 10)$ and $(2\ 0\ 0)$ as a function of temperature. A weak but clear kink at $T_0 = 155$ K is observed for the $(0\ 0\ 10)$ reflection, while no noticeable anomaly appears for the $(2\ 0\ 0)$ reflection. Accordingly, as shown in the Supplementary Fig. 2b, the temperature dependence of the c-axis lattice parameter (c) exhibits an anomaly at $T_0 = 155$ K, whereas the a-axis lattice parameter (a) changes monotonically across T_0. This is consistent with the previous reports [1–3] and also the refinement result on single crystal X-ray diffraction data, taken at 93 K $(< T_0)$. Therefore, the tetragonal symmetry of Sr_2VO_3FeAs remains unchanged below T_0 within experimental resolution. For other iron pnictides showing an orthorhombic distortion, the orthorhombicity $\delta = (a-b)/(a+b)$ is typically $0.5-4 \times 10^{-3}$ [4–7]. Considering that the beam divergence of our single crystal X-ray diffractometer is less than ≈ 0.1 degree, the orthorhombicity, if any, should be less than $\delta \sim 10^{-4}$ in Sr_2VO_3FeAs, at least one order of magnitude smaller than found in other iron pnictides. These observations suggest that the nematic C_2 order is either absent or strongly suppressed in Sr_2VO_3FeAs, highly distinct from other iron pnictides. One can argue that the coupling with the $SrVO_3$ layers hardens the Fe lattice. Indeed our density functional theory (DFT) calculations for a putative stripe order produced an optimized structure with $b/a-1 \lesssim 0.5\%$, while similar calculations for $BaFe_2As_2$ yield 1.5%. Still, it is factor of three short of the observed order-of-magnitude difference.

On the contrary, the c-axis lattice parameter suddenly decreases at T_0 by $\Delta c \approx -0.03$ Å. The reduction is comparable with the orthorhombic distortion $a-b \approx 0.02$ Å in other iron pnictides showing a C_2 structural transition. As discussed in the main text, we attribute this reduction of the c-axis lattice parameter to the anion-height change due to an

Supplementary Table 1: Selected crystallographic information from the structure refinement of the XRD patterns of a Sr_2VO_3FeAs single crystal. The standard deviations of the last digit are given in parentheses. The R values for the Rietveld refinement are $R_{int} = 0.0931$, $R1 = 0.0512$, and $wR2 = 0.0671$.

Data collection temperature [K]		293(2)	93(2)
Space group		$P4/nmm$	$P4/nmm$
Formula units per unit cell	Z	2	2
Lattice parameters [Å]	a	3.9155(7)	3.9105(6)
	c	15.608(4)	15.5077(3)
Unit cell volume [Å^3]	V	239.29(9)	237.14(1)
Calculated density [g · cm^3]	ρ	5.620	5.653
Radiation, wavelength [Å]	λ	Ag-K, 0.56083	
Monochromator		curved graphite single crystal	
Atomic parameters			
Sr(1)	[2c (1/4, 1/4, z)]	0.58642(9)	0.58690(8)
Sr(2)	[2c (1/4, 1/4, z)]	0.81000(8)	0.81081(7)
V(1)	[2c (1/4, 1/4, z)]	0.30763(18)	0.30648(15)
O(1)	[4f (3/4, 1/4, z)]	0.2935(5)	0.2926(7)
O(2)	[2c (1/4, 1/4, z)]	0.4291(7)	0.4301(10)
Fe(1)	[2a (3/4, 1/4, z)]	0	0
As(1)	[2c (1/4, 1/4, z)]	0.08954(10)	0.08941(9)

C_4-symmetry vestigial charge or orbital ordering as discussed in the main text. Our DFT calculation have shown, for instance, that the "double-Q" configuration with half Fe atoms magnetic converges to a structure with the lattice parameter c roughly 0.03 Å lower than in fully magnetic stripe phase.

Supplementary Note 2. Magnetic properties of Sr_2VO_3FeAs single crystals

Above T_0, the magnetic susceptibility follows the Curie-Weiss law expressed by $\chi(T) = C/(T - T_{CW}) + \chi_0$ as shown in the Supplementary Fig. 3a. Here T_{CW} is the Curie-Weiss temperature, and χ_0 is the contribution from itinerant Fe electrons, which in other iron pnictides exhibits a temperature-independent or weakly-dependent behavior[8–10]. C is
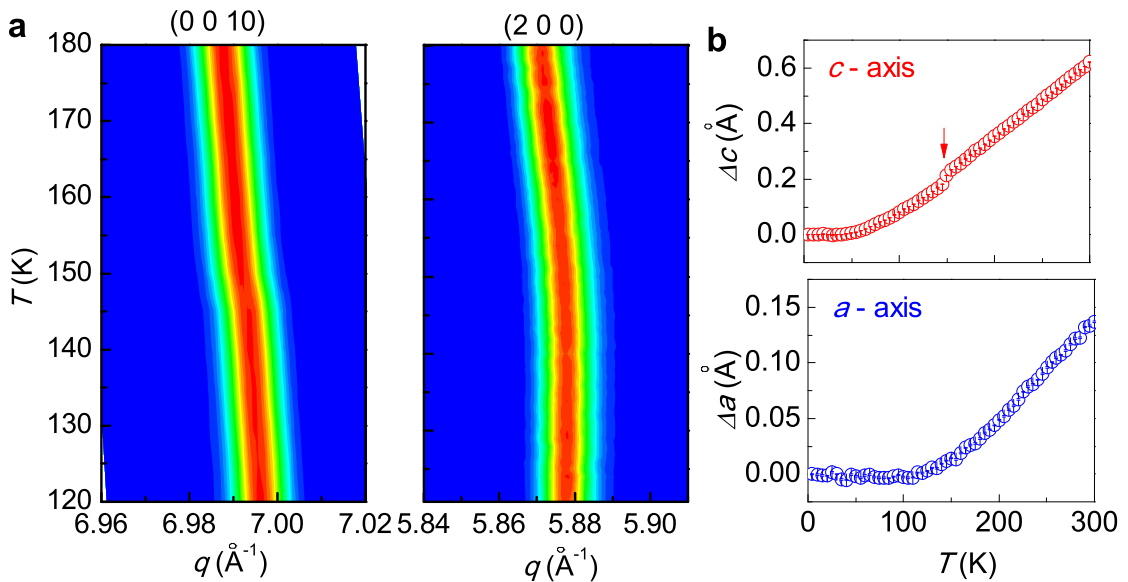
Supplementary Fig. 2: **a** Single crystal X-ray diffraction data from the (0 0 12) and (2 0 0) Bragg peaks as function of temperature. **b** Temperature dependence of the relative change in the a- and c-axis lattice parameters. An anomaly in the c-parameter at T_0 is marked by the arrow.
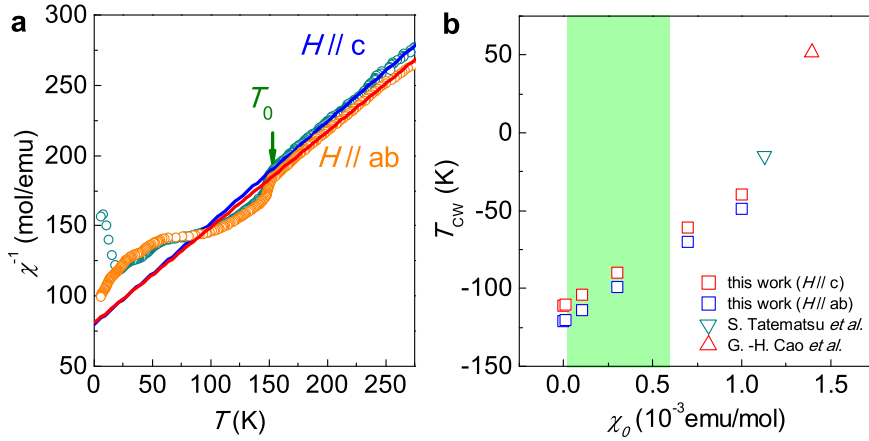
Supplementary Fig. 3: **a** The inverse magnetic susceptibility, $\chi^{-1}(T)$, as a function of temperature for $H\|c$ and $H\|ab$. The hidden order transition at T_0 is indicated by the arrow. The solid lines are the fit to the Curie-Weiss law. **b** The estimated Curie-Weiss temperature T_{CW} with variation of χ_0. The typical χ_0 value for doped iron pnictides is indicated by green shadow.

the molar Curie constant, $C = (NP_{eff}^2)/3k_B$, with the Avogadro's number N and molar effective magnetic moment P_{eff}. The magnitude of χ_0 is typically $\sim 10^{-4}$ emu/mol, smaller by two orders of magnitude than the observed $\chi(T)$ in Supplementary Fig. 3a. Assuming negligible χ_0, we can fit the experimental data well enough, yielding the Curie-Weiss temperature $T_{CW} = -110(1)$ K for $H \parallel c$ and $T_{CW} = -119(2)$ K for $H \parallel ab$. The estimated effective magnetic moments $P_{eff} = (3k_BC/N)^{1/2}$ from the fit are 2.35 μ_B/V for $H\|c$ and 2.43 μ_B/V for $H \parallel ab$. These values are comparable with the expected value $P_{eff} = g\sqrt{S(S+1)}\mu_B = 2.83\mu_B$ for $S = 1$ spins in V^{3+} ions of the $SrVO_3$ layer. The slight reduction of the measured P_{eff} can be attributed to hybridization.

The Curie-Weiss behavior from the localized V spins dominates the temperature dependence of $\chi(T)$. For typical doped iron pnictides without a long-range order [8–11] χ is less than $\sim 0.7 \times 10^{-3}$ emu/mol and very weakly $T-$dependent. We tried several value of χ_0 within this range and obtained the T_{CW} values of -100 ± 30 K, as shown in Supplementary Fig. 3b. For comparison we also plot the T_{CW} estimates in previous reports [1, 2]. Note that the studies reporting a nearly zero or positive T_{CW} utilized $\chi_0 \approx 1.2 - 2.0 \times 10^{-3}$ emu/mol, much larger than typical values for iron pnictides. Setting χ_0 as a fitting parameter, we obtained a slightly better fit to the data, yielding $T_{CW} = -72(2)$ K and $\chi_0 = 0.54(3) \times 10^{-3}$ emu/mol.

Supplementary Note 3. ^{75}As NMR spectra and their analysis for Sr_2VO_3FeAs in a magnetic field $H \parallel (110)$

Supplementary Fig. 4 shows ^{75}As NMR spectra as a function of temperature for field orientations parallel to c (001) and the (110) directions, which were taken on a different single crystal of Sr_2VO_3FeAs. For $H \parallel c$, a sudden change in the Knight shift occurs at $T_0 \approx 155$ K, consistent with the results shown in Fig. 2 of the main text. For $H \parallel (110)$ we obtained the sudden shift of the NMR peak to high frequencies, similar to the results in $H \parallel a$. Neither peak splitting nor broadening were detected as shown in Supplementary Figs. 4c and 4d.

Supplementary Note 4. Comparison with the ^{75}As NMR behavior in other iron-based superconductors

In iron pnictides or chalcogenides, various types of the long-range spin and orbital orders are stabilized in parent compounds such as $LaFeAsO$ and $BaFe_2As_2$. The most common parent phases are the C_2 orbital (nematic) order and the stripe-type C_2 antiferromagnetic (AFM) order [12]. The C_2 orbital order at T_S usually precedes the C_2 magnetic order at T_N ($T_S \geq T_N$), and depending on the coupling strength between these orders, their ordering temperatures differ in a wide range [13]. The most extreme case is $FeSe$ where only a C_2 orbital ordering occurs, at $T_S = 90$ K, whereas the C_2 spin correlation fails to induce the static magnetic order [14]. There are some exceptions, however, exhibiting different types of AFM or orbital-ordered phases such as a bicollinear-AFM in $FeTe$ [15], a double-Q C_4-AFM in $(Ba,Na)Fe_2As_2$ and $(Ba,K)Fe_2As_2$ [16–18], and a spin-reoriented-AFM orders in $Ba_{0.65}Na_{0.35}Fe_2As_2$ [19] as
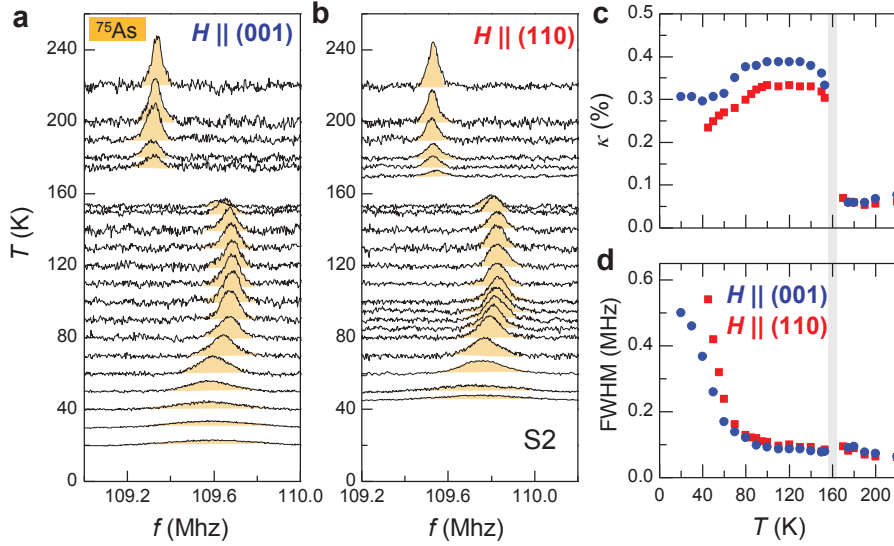
Supplementary Fig. 4: ^{75}As NMR spectra as a function of temperature, measured at $H = 15$ T at different field orientations **a** $H||(001)$ **b** $H||(110)$, respectively. Temperature dependence of **c** Knight shift and **c** linewidth for ^{75}As NMR spectra. The ^{75}As NMR spectra as a function of temperature for field orientations parallel to a (100) and the (110) direction show almost consistent behavior.

listed in the Supplementary Table 2.

This also includes the nonmagnetic collapsed C_4 phase in rare-earth doped $CaFe_2As_2$ as discussed in the supplementary section 1. These ground states have their own characteristic temperature dependences in the Knight shift and the spin-lattice relaxation rate $1/T_1T$, depending on the underlying spin or orbital structures, which can be categorized as shown in Supplementary Fig. 5. The observed NMR properties of Sr_2VO_3FeAs are highly distinct from those in other iron-pnictides or chalcogenides. Particularly, the spin pseudogap behavior, *i.e.*, dramatic suppression of $1/T_1T$ is a precursor of the C_4 symmetric order at T_0, as discussed in the main text, reflecting the unique role of the interfacial Fe-V interaction in the hetero-structured Sr_2VO_3FeAs.

Supplementary Table 2: Representative antiferromagnetic and orbital-ordered phases considered for iron pnictides and chalcogenides. The patterns of the orbital and spin orders, the corresponding transition temperatures (T_S) and T_N), and the behavior of NMR properties are listed in Supplementary Fig. 5.

Family	Compounds	Electronic ground state				NMR results
		Orbital		Spin		
11	FeSe	C_2	$T_S \sim 90$ K	-	-	**a** [14]
	FeTe [15]	C_2	$T_S \sim 67$ K	Bicollinear-AFM	-	-
111	NaFeAs	C_2	$T_S \sim 49$ K	C-type AFM	$T_N \sim 39$ K	**b** [20]
	LiFeAs	-	-	-	-	-
122	$BaFe_2As_2$	C_2	$T_S \sim 142$ K	C-type AFM	$T_N \sim 143$ K	**b** [21, 22]
	$SrFe_2As_2$	C_2	$T_S \sim 173$ K	C-type AFM	$T_N \sim 220$ K	**b** [23]
	$(Ca,Pr)Fe_2As_2$	Collapsed-C_4	$T_S \sim 65$ K	-	-	**c** [24, 25]
	$(Ba,Na)Fe_2As_2$ [26]	C_2	$T_{S1} \sim 80$ K	Double-Q AF in C_4-lattice	$T_{N1} \sim 80$ K	-
		C_4	$T_{S2} \sim 50$ K	Spin-reoriented C_4	$T_{N2} \sim 50$ K	-
1111	LaFeAsO	C_2	$T_S \sim 155$ K	C-type AFM	$T_N \sim 137$ K	**b** [27]
	LaFeAs(O,H)	C_2	$T_S \sim 95$ K	C-type AFM	$T_N \sim 89$ K	**b** [28]
21311	$Ca_2AlO_3Fe(As,P)$	-	-	AFM	$T_N \sim 70$ K	**b** [29]
	$Sr_2(Mg,Ti)O_3FeAs$	-	-	AFM	$T_N \sim 50$ K	**b** [30]
	Sr_2ScO_3FeAs [31]	-	-	AFM	$T_N \sim 35$ K	-
21311	Sr_2VO_3FeAs (our work)	C_4	$T_0 \sim 155$ K	Spin-gap-like	$T_{sg} \sim 220$ K	**d**
				C_4-AFM	$T_N \sim 45$ K	
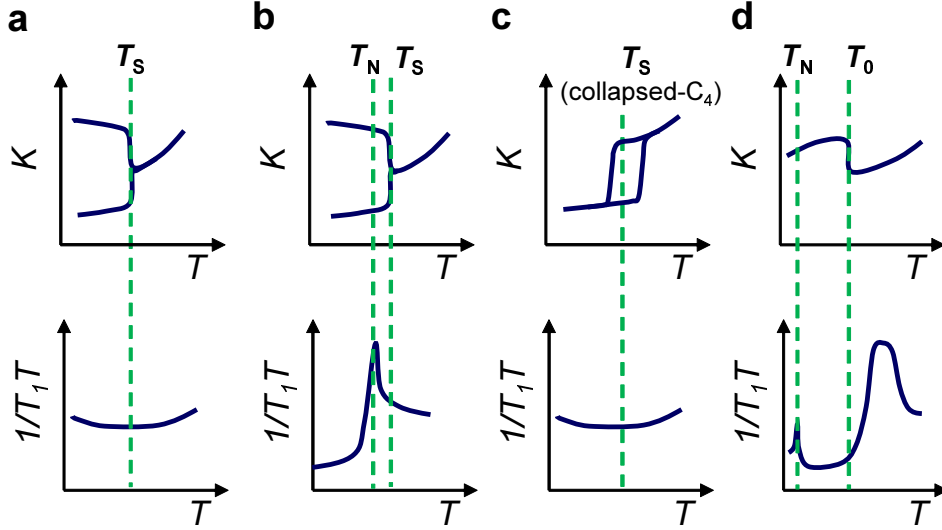
Supplementary Fig. 5: A cartoon illustration of various types of the temperature variation of the Knight shift(K) and the spin-lattice relaxation rate ($1/T1T$) in iron pnictides and chalcogenides. **a** The C_2 orbital ordered phase without any static AFM order in FeSe. **b** The C_2 orbital-ordered and AFM phases, the most commonly observed parent phase in AFe$_2$As$_2$, ReOFeAs, and A_2MO_3FeAs (A = alkaline earths, Re = rare earths, M = nonmagnetic metals). **c** The collapsed C_4 phase in (Ca,Re)Fe$_2$As$_2$. **d** Putative C_4 orbital-ordered and AFM phases in Sr$_2$VO$_3$FeAs (this work).

Supplementary Note 5. ^{75}As NMR peak splitting in ordered phases of iron pnictides

Symmetry analysis of the hyperfine coupling tensor. As described in Ref. [21], the hyperfine coupling between ^{75}As nucleus and Fe moments has different characters, depending on the symmetry breaking by the underlying spin/orbital orders. Since the As site is located above and below the center of Fe plaquette in the square lattice, the hyperfine field at the As site, H^{hf}, is determined by adding the contribution of the surrounding four Fe spins as expressed by

$$H_i^{hf} = \sum_{j\alpha\beta} B_{ij}^{\alpha\beta} s_j^{\alpha\beta}, \tag{1}$$

where i, j are Cartesian indices, x (a), y (b) or z (c), $\mathbf{s}^{\alpha\beta}$ is the spin at the plaquette site $\alpha\beta$, where $\alpha\beta$ takes four values $\pm 1, \pm 1$. $\hat{\mathbf{B}}^{\alpha\beta}$ is the hyperfine coupling tensor between the As nucleus and Fe moments at the $\alpha\beta$ site which can be given by symmetry rotations,

$$B_{ij}^{\alpha\beta} = e_i^{\alpha\beta} B_{ij}^0 e_j^{\alpha\beta}, \tag{2}$$

$$e^{++} = (1, 1, 1); \ e_i^{+-} = (1, -1, 1); \ e_i^{-+} = (-1, 1, 1); \ e_i^{--} = (-1, -1, 1). \tag{3}$$

Here, $\hat{\mathbf{B}}^0$ can be written using explicitly the underlying tetragonal symmetry,

$$\hat{\mathbf{B}}^0 = \begin{pmatrix} B_{aa} & B_{ab} & B_{ac} \\ B_{ba} & B_{bb} & B_{bc} \\ B_{ca} & B_{cb} & B_{cc} \end{pmatrix} = \begin{pmatrix} X & U & V \\ U & X & V \\ V & V & Z \end{pmatrix}. \tag{4}$$

For collinear structures, $\mathbf{s}^{\alpha\beta} = \sigma^{\alpha\beta}\mathbf{s}$, where $\mathbf{s} = (s_a, s_b, s_c)$. Then the formula can by simplified further as

$$H_i^{hf}(\mathbf{s}||j) = \sum_{\alpha\beta} e_i^{\alpha\beta} B_{ij}^0 e_j^{\alpha\beta} \sigma^{\alpha\beta} \mathbf{s} = B_{ij}^0 T_{ij} \mathbf{s}, \tag{5}$$

$$T_{ij} = \sum_{\alpha\beta} e_i^{\alpha\beta} e_j^{\alpha\beta} \sigma^{\alpha\beta} = \sum_{\alpha\beta} t_{ij}^{\alpha\beta} \sigma^{\alpha\beta}, \tag{6}$$

where the matrix T carries all information about a particular magnetic pattern. Here, the matrices t are

$$t^{++} = \begin{pmatrix} 1 & 1 & 1 \\ 1 & 1 & 1 \\ 1 & 1 & 1 \end{pmatrix} \; ; \; t^{+-} = \begin{pmatrix} 1 & -1 & 1 \\ -1 & 1 & -1 \\ 1 & -1 & 1 \end{pmatrix} \; ; \; t^{-+} = \begin{pmatrix} 1 & -1 & -1 \\ -1 & 1 & 1 \\ -1 & 1 & 1 \end{pmatrix} \; ; \; t^{--} = \begin{pmatrix} 1 & 1 & -1 \\ 1 & 1 & -1 \\ -1 & -1 & 1 \end{pmatrix} . \tag{7}$$

Spin order	Hyperfine field H^{hf}	Number of peaks		

Stripe

$H^{hf} = \pm 4V \begin{pmatrix} s_c \\ 0 \\ s_a \end{pmatrix}$ ($\blacklozenge$, $\lozenge$) ($\bullet$, $\circ$)

	$H\|a$	$H\|b$	$H\|c$
$s\|a$	1	1	2
$s\|b$	1	1	1
$s\|c$	2	1	1

Neel

$H^{hf} = \pm 4U \begin{pmatrix} s_b \\ s_a \\ 0 \end{pmatrix}$ ($\blacklozenge$) ($\circ$)

	$H\|a$	$H\|b$	$H\|c$
$s\|a$	1	2	1
$s\|b$	2	1	1
$s\|c$	1	1	1

Non-uniform/ double-Q

$H^{hf} = \pm \begin{pmatrix} 2Vs_c \\ -2Vs_c \\ 2Vs_a - 2Vs_b \end{pmatrix}$ ($\square$, $\star$)

$H^{hf} = \pm \begin{pmatrix} 2Vs_c \\ 2Vs_c \\ 2Vs_a + 2Vs_b \end{pmatrix}$ ($\bullet$, $\blacklozenge$)

	$H\|a$	$H\|b$	$H\|c$
$s\|a$	1	1	2
$s\|b$	1	1	2
$s\|c$	2	2	1

Bi-collinear

$H^{hf} = \pm \begin{pmatrix} 2Xs_a + 2Us_b - 2Vs_c \\ 2Us_a + 2Xs_b + 2Vs_c \\ -2Vs_a + 2Vs_b + 2Zs_c \end{pmatrix}$ ($\blacksquare$, $\bullet$)

$H^{hf} = \pm \begin{pmatrix} -2Xs_a - 2Us_b - 2Vs_c \\ -2Us_a - 2Xs_b + 2Vs_c \\ -2Vs_a + 2Vs_b - 2Zs_c \end{pmatrix}$ ($\star$, $\lozenge$)

	$H\|a$	$H\|b$	$H\|c$
$s\|a$	2	2	2
$s\|b$	2	2	2
$s\|c$	2	2	2

Plaquette

$H^{hf} = \pm \begin{pmatrix} 4Xs_a \\ 4Xs_b \\ 4Zs_c \end{pmatrix}$ ($\blacksquare$, $\bullet$)

$H^{hf} = \pm \begin{pmatrix} 4Vs_c \\ 0 \\ 4Vs_a \end{pmatrix}$ ($\diamondsuit$, $\star$)

$H^{hf} = \pm \begin{pmatrix} 4Us_b \\ 4Us_a \\ 0 \end{pmatrix}$ ($\triangleleft$, $\clubsuit$)

$H^{hf} = \pm \begin{pmatrix} 0 \\ 4Vs_c \\ 4Vs_b \end{pmatrix}$ ($\blacklozenge$, $\heartsuit$)

	$H\|a$	$H\|b$	$H\|c$
$s\|a$	5	5	5
$s\|b$	5	5	5
$s\|c$	5	5	5

Supplementary Fig. 6: Schematic spin configurations of various antiferromagnetic (AFM) orders in iron pnictides and the corresponding hyperfine field (H_{hf}) at the As sites. Four neighboring Fe spins, s_i $(i = 1,2,3,4)$, determining the H^{hf} at the As site in the center are indicated by arrows on top of the larger open circles as shown in the case of the stripe AFM. The same indexing scheme of s_i is used for calculating H^{hf} at the different As sites, indicated by smaller symbols, above (solid) and below (open) the Fe square lattice. The resulting NMR line splitting is also given for different orientations of spin s and external magnetic field H along the a, b, c axes.

NMR line splitting due to antiferromagnetic orders. In a magnetically ordered state, the Fe spins on an Fe_4 plaquette have a particular ordering, as illustrated in Supplementary Fig. 6. For example, in the stripe AFM state with the in-plane wave vector $\mathbf{Q} \approx (0, \pi)$, $\sigma^{\alpha\beta}$ can be expressed as $\begin{pmatrix} 1 & -1 \\ 1 & -1 \end{pmatrix}$. Accordingly, the characteristic matrix T and the corresponding hyperfine field H^{hf} are

$$T = \begin{pmatrix} 0 & 0 & 0 \\ 0 & 0 & 4 \\ 0 & 4 & 0 \end{pmatrix}; H^{hf} = \pm 4V \begin{pmatrix} s_c \\ 0 \\ s_a \end{pmatrix}. \tag{8}$$

Based on the above calculations, a stripe AFM with spin moments along the a-axis ($s \parallel a$) results in an internal hyperfine field along the c-axis. Thus the As nuclei, located above ($\bullet, \blacklozenge$ in Supplementary Fig. 6) and below ($\circ, \Diamond$ in Supplementary Fig. 6) the Fe plane, will experience the opposite internal hyperfine fields along the c-axis. When the external magnetic field H is applied along the c-axis ($H \parallel c$), the total field at each As site is $H_{tot} = H \pm 4Vs$, which leads to two NMR peaks at different frequencies of $f = \gamma H_{tot} = \gamma(H \pm 4Vs)$. In contrast, with an external field along the a (or b) axis ($H \parallel a$ or $H \parallel b$), only one NMR peak is observed at a frequency $f = \gamma H_{tot} = \gamma\sqrt{H^2 + (4Vs)^2}$. Using the similar symmetry analysis, we can obtain the NMR frequency (f) induced by the stripe AFM orders with different orientations of the Fe spins ($s \parallel a$, $s \parallel b$, or $s \parallel c$) and external magnetic field orientations ($H \parallel a, H \parallel b, H \parallel c$), as summarized in the first panel of Supplementary Fig. 6. Following the same procedure, one can determine the net hyperfine coupling tensor ($B_{ij}^0 T_{ij}$), and the net hyperfine field (H^{hf}) at the As sites for various types of the AFM phases with different spin configurations and also for different spin orientations, as listed in Supplementary Fig. 6.

For Neel-type correlations with $\mathbf{Q} \approx (\pi, \pi)$, the $\sigma^{\alpha\beta}$ is $\begin{pmatrix} + & - \\ - & + \end{pmatrix}$, and the corresponding matrix T and hyperfine field H^{hf} are

$$T = \begin{pmatrix} 0 & 4 & 0 \\ 4 & 0 & 0 \\ 0 & 0 & 0 \end{pmatrix}; H^{hf} = \pm 4U \begin{pmatrix} s_b \\ s_a \\ 0 \end{pmatrix}. \tag{9}$$

For the double-$\mathbf{Q}$ fluctuations with $\mathbf{Q} \approx (\pi, 0), (0, \pi)$, two possible magnetic patterns are expected. Thus, the $\sigma^{\alpha\beta}$ for possible patterns are $\begin{pmatrix} 0 & + \\ - & 0 \end{pmatrix}$ and $\begin{pmatrix} + & 0 \\ 0 & - \end{pmatrix}$. The corresponding matrices T the hyperfine field H^{hf} at different sites are

$$T = \begin{pmatrix} 0 & 0 & 2 \\ 0 & 0 & -2 \\ 2 & -2 & 0 \end{pmatrix}, \begin{pmatrix} 0 & 0 & 2 \\ 0 & 0 & 2 \\ 2 & 2 & 0 \end{pmatrix}, \tag{10}$$

and

$$H^{hf} = \pm 2V \begin{pmatrix} s_c \\ -s_c \\ s_a - s_b \end{pmatrix}; \pm 2V \begin{pmatrix} s_c \\ s_c \\ s_a + s_b \end{pmatrix}. \tag{11}$$

For bi-collinear correlations, $\mathbf{Q} \approx (\pi, \pi)$, the possible patterns are $\begin{pmatrix} + & - \\ + & + \end{pmatrix}$ and $\begin{pmatrix} - & - \\ + & - \end{pmatrix}$. The corresponding matrices T the hyperfine field H^{hf} at different sites are

$$T = \begin{pmatrix} 2 & 2 & -2 \\ 2 & 2 & 2 \\ -2 & 2 & 2 \end{pmatrix}, \begin{pmatrix} -2 & -2 & -2 \\ -2 & -2 & 2 \\ -2 & 2 & -2 \end{pmatrix}, \tag{12}$$

and

$$H^{hf} = \pm 2 \begin{pmatrix} Xs_a + Us_b - Vs_c \\ Us_a + Xs_b + Vs_c \\ -Vs_a + Vs_b + Zs_c \end{pmatrix}; \pm 2 \begin{pmatrix} -Xs_a - Us_b - Vs_c \\ -Us_a - Xs_b + Vs_c \\ -Vs_a + Vs_b - Zs_c \end{pmatrix}. \tag{13}$$

For plaquette correlation, there are four patterns, $\begin{pmatrix} + & + \\ + & + \end{pmatrix}$, $\begin{pmatrix} + & + \\ - & - \end{pmatrix}$ and $\begin{pmatrix} + & - \\ + & - \end{pmatrix}$, and $\begin{pmatrix} + & - \\ - & + \end{pmatrix}$.

The corresponding matrices T the hyperfine field H^{hf} at different sites are

$$T = \begin{pmatrix} 4 & 0 & 0 \\ 0 & 4 & 0 \\ 0 & 0 & 4 \end{pmatrix}, \begin{pmatrix} 0 & 0 & 4 \\ 0 & 0 & 0 \\ 4 & 0 & 0 \end{pmatrix}, \begin{pmatrix} 0 & 4 & 0 \\ 4 & 0 & 0 \\ 0 & 0 & 0 \end{pmatrix}, \begin{pmatrix} 0 & 0 & 0 \\ 0 & 0 & 4 \\ 0 & 4 & 0 \end{pmatrix}, \tag{14}$$

and

$$H^{hf} = \pm 4 \begin{pmatrix} X s_a \\ X s_b \\ Z s_c \end{pmatrix}; \pm 4V \begin{pmatrix} s_c \\ 0 \\ s_a \end{pmatrix}; \pm 4U \begin{pmatrix} s_b \\ s_a \\ 0 \end{pmatrix}; \pm 4V \begin{pmatrix} 0 \\ s_c \\ s_b \end{pmatrix}. \tag{15}$$

Now we discuss the possible $75^A s$ NMR line splitting for various types of AFM orders, which have been identified experimentally or suggested theoretically in iron pnictides, including the stripe-AFM, the bicollinear-AFM, the double-Q C_4-AFM, the spin-reoriented-AFM, the non-collinear AFM, and the plaquette AFM orders. As summarized in Supplementary Fig. 6, in some cases with a small magnetic unit cell, such as stripe or Neel orders, the hyperfine field H^{hf} points along either the a or c axes, which results in NMR line splitting for either $H \parallel c$ or $H \parallel a$. In some cases, such as bicollinear and plaquette AFM orders, there are more than two inequivalent As sites having different hyperfine coupling tensors and thus different net H^{hf} fields along the a or c axes. Then this results in an NMR line splitting under both $H \parallel c$ and $H \parallel a$, which is not consistent with the experimental results for Sr_2VO_3FeAs. There are only two cases where no hyperfine field is generated on the As site, namely, the stripe AFM phase with the spins aligned in-plane and normal to the AFM ordering vector ($\mathbf{s} \perp \mathbf{Q} = (1,0)$) and the Neel AFM phase with the out-of-plane spins ($\mathbf{s} \| c$). In this case no splitting of the As NMR line is expected. However even in this case (as in any other magnetically-ordered state) we should have observed considerable peak broadening of ^{75}As NMR spectra due to the directional fluctuation of Fe spins in the AFM phase or a diverging behavior of $1/T_1T$ across T_0, which were not observed in the experiments. Therefore, we can conclude that no long-range magnetic order emerges at T_0.

NMR peak splitting due to nematic orders. Even without a long-range magnetic order, the NMR line splitting can be induced when the local symmetry at the As site is broken in the nematic phases. As described in the case of FeSe [14], the Knight shifts $K_{\alpha\alpha} = A^{hf}_{\alpha\alpha}\chi_{\alpha\alpha}$ ($\alpha = x, y, z$) is affected by the nematic order, which breaks the in-plane rotational symmetry and introduces two non-equivalent directions in the plane. In this case, as the spin fluctuation or orbital occupation becomes anisotropic in the plane, indicated by the d_{xz} or d_{yz} orbital in Supplementary Fig. 7, the spin susceptibility (χ) or the hyperfine coupling (A^{hf}) at the As site also become anisotropic, i.e., $\chi_{xx} \neq \chi_{yy}$ and/or $A^{hf}_{xx} \neq A^{hf}_{yy}$. In this case, the isotropic (K_{av}) and anisotropic (ΔK) parts of the in-plane Knight shift are given as

$$K_{av} = 1/2(A^{hf}_{xx} + A^{hf}_{yy})(\chi_{xx} + \chi_{yy}) + 1/2(A^{hf}_{xx} - A^{hf}_{yy})(\chi_{xx} - \chi_{yy}), \tag{16}$$

and

$$\Delta K = 1/2(A^{hf}_{xx} + A^{hf}_{yy})(\chi_{xx} - \chi_{yy}) + 1/2(A^{hf}_{xx} - A^{hf}_{yy})(\chi_{xx} + \chi_{yy}). \tag{17}$$

For example, in the conventional stripe nematic order, the x and y directions are aligned along one of the crystallographic directions, e.g, $x \parallel a$ and $y \parallel b$. In this detwinned case, there is one equivalent As site, and thus As NMR line will be shifted differently for $H \parallel a$ and $H \parallel b$. In reality, when external magnetic field is applied e.g. $H \parallel a$, crystals are twined with two domains of $H \parallel a$ and $H \parallel b$ as the stripe nematic order develops, which results in the As NMR line splitting. For $H \parallel (110)$, on the other hand, the isotropic part, dominated by the average susceptibility, $1/2(\chi_{xx} + \chi_{yy})$, and the average hyperfine coupling constant, $1/2(A^{hf}_{xx} + A^{hf}_{yy})$, is measured, which turns out to be almost the same across the stripe nematic transition, as experimentally confirmed in FeSe and also in LaFeAsO. This behavior is not consistent with what observed in Sr_2VO_3FeAs as shown in Fig. 2 of the main text.

We can consider nematic or vestigial phases corresponding to other types of AFM spin orders, in the same spirit as the standard C_2 nematicity, breaking the C_4 tetragonal symmetry but preserving the $O(3)$ spin-rotational symmetry, is a "vestige" of the stripe AFM phase. For examples, one can consider vestigial phases corresponding to the more complex AFM phases, such as bicollinear or plaquette AFM orders. For the bicollinear nematic phase, the C_4 tetragonal symmetry is broken by the next-nearest neighbor bond order along the diagonal direction of the Fe square lattice, indicated by the blue oval in Supplementary Fig. 7. This order must trigger an orbital order with different

occupations between d_{xz+yz} and d_{xz-yz} states. By further developing the nearest neighbor bond order, indicated by the red oval in Supplementary Fig. 7, the reflection and the translation symmetries are broken. In this case, the line splitting is expected for twinned crystals, similar to the stripe nematic case, but not for $H \parallel (100)$ but for $H \parallel (110)$ as summarized in Supplementary Fig. 7. The vestigial phase for the plaquette AFM order has more than one inequivalent As sites, and must trigger an As NMR peak splitting in any magnetic field orientation. Note that in both cases the generated orbital imbalance between the corresponding orbital combinations of Fe $d_{xz} \pm d_{yz}$ is expected to be of the same order of magnitude as in the stripe-nematic case, so also a the peak splitting for $H \parallel (110)$ should be detectable. This is however not observed in experiments.

As a possible candidate we consider the vestigial phase for the double-Q AFM phase, which generate a checkerboard-type combination of two charge density waves. In this case, the charge density for C_4 orbital states such as d_{xy} state is unequal between odd and even sites of the Fe square lattice as shown in Supplementary Fig. 7. Thus the time-reversal and C_4 tetragonal symmetries are preserved, but the translational symmetry is broken by unit-cell doubling in the Fe-only lattice. Note however that this unit-cell doubling exactly matches the unit-cell doubling due the As sites above and below the Fe square lattice. Thus the vestigial phase for the nonuniform double-Q phase has a C_4 symmetric and intra-unit-cell order in the FeAs layers.

In this case, each As then has two nonmagnetic Fe neighbors, and two paramagnetic, with non-zero local moments

	Nematic order	Orbital order	Number of peaks			
			detwinned		twinned	
Stripe			$H\|\|(100)$ $H\|\|(110)$ 1 1		$H\|\|(100)$ $H\|\|(110)$ 2 1	
Bi-collinear			$H\|\|(100)$ $H\|\|(110)$ 1 1		$H\|\|(100)$ $H\|\|(110)$ 1 2	
Plaquette			$H\|\|$any directions 2		$H\|\|$any directions 2	
Non-uniform/ double-Q			$H\|\|(100)$ $H\|\|(110)$ 1 2		$H\|\|(100)$ $H\|\|(110)$ 1 2	
d_{xy} orbital	**Orbital -selective Mott**		$H\|\|(100)$ $H\|\|(110)$ 1 1		$H\|\|(100)$ $H\|\|(110)$ 1 1	

Supplementary Fig. 7: Schematic illustration of various nematic orders and the possible accompanying orbital orders in iron pnictides. The nearest (next-nearest) neighbor ferromagnetic bonds are indicated by thick red (blue) ovals. For the double-Q nematic order, the magnetically active sites are indicated by filled (orange) circles; their charge and/or orbital state can differ from that of the nonmagentic (open circles) states. For the orbital selective Mott-state, the orbital population of each state is the same but different from that in the high-temperature phase. We illustrated orbital ordering by drawing an orbital whose population could be different above and below the transition. The expected number of the As NMR frequencies for detwinned/twinned crystal are listed for each relevant external field orientation.

that are fluctuating so as to preserve short-range spin correlations among themselves. This affects the Fe-As hybridization and modifies the ^{75}As Knight shift as observed in our experiments (Fig. 2 and Supplementary Fig. 4). Strictly speaking, the ^{75}As line splitting could occur for a field parallel to (110), since half of As in this phase have paramagmetic neighbors along (110), and half along (1$\bar{1}$0). However, we observed the ^{75}As line shift nearly independent on the filed directions, indicating that it results from the change of the isotropic Fermi-contact and core-polarization terms, and not dipole or orbital ones. Therefore it is likely that the signal is dominated by the former interaction, in which case the expected splitting can be vanishingly small, below the experimental resolution.

Indirect support to this scenario comes from LDA+DMFT calculations, which can address the difference between the paramagnetic and nonmagnetic Fe, since they account for local spin fluctuation (albeit not short-range correlations). In typical FeSCs, the relative d-orbital occupation changes slightly ($\sim$ 3-5%) [32], although the average Fe-As hybridization changes. This is also the case of Sr_2VO_3FeAs, in which the d-orbital occupations, obtained by DFT+DMFT calculations, differ by only 4-8% with respect to the DFT results. This is much smaller than the typical difference ($\sim$ 20%) in orbital occupations between d_{xz} and d_{yz} states for the C_2 nematic phases [33]. This observation again supports the idea that the shift of the NMR lines in the vestigial phase may be much larger than it splitting. An advantage of this scenario is that it is driven by the same spin fluctuations at $Q = (0, \pi)$ and $(\pi, 0)$ that are present above T_0 and manifest themselves via critically enhanced relaxation rate $1/T_1T$ above $\sim$ 200 K.

One can envision a fully nonmagnetic phase transition changing orbital occupations at $T_0 = 155$ K, such as an orbital-selective Mott-transition with delocalized d_{xy} bands above T_0 into gapped Hubbard states below. In this case, the orbital occupation of, $e.g.$, d_{xy} states is changes for all the Fe sites, keeping the C_4 symmetry intact, as shown in Supplementary Fig. 7. This would result in a nearly isotropic As NMR peak shift without splitting or broadening, consistent with the experiments. However, it seems somewhat counterintuitive that the critical stripe-like fluctuations observed above the transition disappear without trace at T_0; so far materials that were proposed as candidates for such an orbital-selective Mott transition have been either much more strongly correlated than low-doping pnictides (such as isostructural chalcogenides) or severely underdoped and thus closer to half-filling (KFe_2As_2). At the current stage, it is not clear which is the true order below T_0, the vestigial non-uniform double-Q phase or an orbital-selective Mott transition of C_4 orbitals. Nevertheless, the observed C_4 symmetric and intra-unit-cell order in Sr_2VO_3FeAs is unprecedented in iron pnictides, emphasizing the importance of the interfacial Fe-V interactions in the heterostructure.

Supplementary Note 6. Spin-lattice relaxation rate in the normal state

The spin-lattice relaxation rate can be derived based on the fluctuation-dissipation theorem. The $1/T_1$ is usually described in terms of the hyperfine field fluctuations perpendicular to the external magnetic fields [21, 34, 35].

$$\left(\frac{1}{T_1}\right)_z = \frac{(\mu_0\gamma_N)^2}{2}\int_\infty^{-\infty} dt (<H_{hf,x}(t), H_{hf,x}(0)> + <H_{hf,y}(t), H_{hf,y}(0)>)e^{i\omega_0 t}$$

$$= (\mu_0\gamma_N)^2(|H_{hf,x}(\omega_0)|^2 + |H_{hf,y}(\omega_0)|^2) \tag{18}$$

Each As has four nearest neighbor Fe immediately above or below. Since the magnetic anisotropy in FeSC is at least one order of magnitude weaker that the isotropic coupling, at high temperatures the four Fe spins around an As will fluctuate coherently, respecting a particular pattern, and the the hyperfine field on As will fluctuate correspondingly. For an external field direction $\hat{\mathbf{n}}$ the relaxation rate will be defined by

$$\left(\frac{1}{T_1}\right)_{\hat{\mathbf{n}}} = (\mu_0\gamma_N)^2 \left\langle |\mathbf{H}_{hf}(\omega_0) \times \hat{\mathbf{n}}|^2 \right\rangle \tag{19}$$

Where $\langle\rangle$ is averaging over all possible types of fluctuations. For instance, for the stripe fluctuations we average over two types of spin plaquettes, $\begin{pmatrix} + & - \\ + & - \end{pmatrix}$ and $\begin{pmatrix} + & + \\ - & - \end{pmatrix}$, and over all spin directions (collinear in the plaquette). Let us first do the some rearranging:

$$\left\langle |\mathbf{H}^{hf} \times \hat{\mathbf{n}}|^2 \right\rangle = \sum_{ij} \left\langle (\delta_{ij} - n_i n_j) H_i^{hf} H_j^{hf} \right\rangle_{dir} = \sum_{ij}(\delta_{ij} - n_i n_j) \left\langle H_i^{hf} H_j^{hf} \right\rangle_{dir}, \tag{20}$$

where

$$\left\langle H_i^{hf} H_j^{hf} \right\rangle = \sum_{ijkl\alpha\beta\gamma\delta} B_{ik}^{\alpha\beta} s_k^{\alpha\beta} B_{jl}^{\gamma\delta} s_l^{\gamma\delta} = \sum_k B_{ik}^0 T_{ik} B_{jk}^0 T_{jk}. \tag{21}$$

For AFM stripe spin fluctuations with $\mathbf{Q} \approx (0, \pi)$, $\sigma^{\alpha\beta}$ takes two values, $\begin{pmatrix} + & - \\ + & - \end{pmatrix}$ and $\begin{pmatrix} + & + \\ - & - \end{pmatrix}$. The corresponding matrices T are

$$T = \begin{pmatrix} 0 & 0 & 0 \\ 0 & 0 & 4 \\ 0 & 4 & 0 \end{pmatrix}, \quad \begin{pmatrix} 0 & 0 & 4 \\ 0 & 0 & 0 \\ 4 & 0 & 0 \end{pmatrix}. \tag{22}$$

This immediately gives us

$$\left\langle H_i^{hf} H_j^{hf} \right\rangle = \frac{1}{2} \left[\begin{pmatrix} 16V^2 & 0 & 0 \\ 0 & 0 & 0 \\ 0 & 0 & 16V^2 \end{pmatrix} + \begin{pmatrix} 0 & 0 & 0 \\ 0 & 16V^2 & 0 \\ 0 & 0 & 16V^2 \end{pmatrix} \right] = \begin{pmatrix} 8V^2 & 0 & 0 \\ 0 & 8V^2 & 0 \\ 0 & 0 & 16V^2 \end{pmatrix}. \tag{23}$$

For the in- and out of plane relaxation rate, $(1/T_1)_{H||a} = (1/T_1)_{H||b} \propto Tr \left\langle H_i^{hf} H_j^{hf} \right\rangle - \left\langle H_1^{hf} H_1^{hf} \right\rangle = 24V^2$, $(1/T_1)_{H||c} \propto Tr \left\langle H_i^{hf} H_j^{hf} \right\rangle - \left\langle H_3^{hf} H_3^{hf} \right\rangle = 16V^2$, the anisotropy ratio is thus 1.5, as has been experimentally observed in many FeSCs.

For Neel-type correlations, $\mathbf{Q} \approx (\pi, \pi)$, the only possible pattern is $\begin{pmatrix} + & - \\ - & + \end{pmatrix}$,

$$T = \begin{pmatrix} 0 & 4 & 0 \\ 4 & 0 & 0 \\ 0 & 0 & 0 \end{pmatrix}, \tag{24}$$

$$\left\langle H_i^{hf} H_j^{hf} \right\rangle = \begin{pmatrix} 16V^2 & 0 & 0 \\ 0 & 16V^2 & 0 \\ 0 & 0 & 0 \end{pmatrix}, \tag{25}$$

and $(1/T_1)_{H||a} = (1/T_1)_{H||b} \propto Tr \left\langle H_i^{hf} H_j^{hf} \right\rangle - \left\langle H_1^{hf} H_1^{hf} \right\rangle = 16V^2$, $(1/T_1)_{H||c} \propto Tr \left\langle H_i^{hf} H_j^{hf} \right\rangle - \left\langle H_3^{hf} H_3^{hf} \right\rangle = 32V^2$, the anisotropy ratio is 0.5.

For the double-$\mathbf{Q}$ fluctuations both wave vectors are excited equally, $\mathbf{Q} \approx (\pi, 0), (0, \pi)$, the possible patterns are $\begin{pmatrix} 0 & - \\ + & 0 \end{pmatrix}$ and $\begin{pmatrix} + & 0 \\ 0 & - \end{pmatrix}$,

$$T = \begin{pmatrix} 0 & 0 & -2 \\ 0 & 0 & 2 \\ -2 & 2 & 0 \end{pmatrix}, \quad \begin{pmatrix} 0 & 0 & 2 \\ 0 & 0 & 2 \\ 2 & 2 & 0 \end{pmatrix}, \tag{26}$$

$$\left\langle H_i^{hf} H_j^{hf} \right\rangle = \frac{1}{2} \left[\begin{pmatrix} 4V^2 & 4V^2 & 0 \\ 4V^2 & 4V^2 & 0 \\ 0 & 0 & 8V^2 \end{pmatrix} + \begin{pmatrix} 4V^2 & -4V^2 & 0 \\ -4V^2 & 4V^2 & 0 \\ 0 & 0 & 8V^2 \end{pmatrix} \right] = \begin{pmatrix} 4V^2 & 0 & 0 \\ 0 & 4V^2 & 0 \\ 0 & 0 & 8V^2 \end{pmatrix}. \tag{27}$$

$(1/T_1)_{H||a} = (1/T_1)_{H||b} \propto Tr \left\langle H_i^{hf} H_j^{hf} \right\rangle - \left\langle H_1^{hf} H_1^{hf} \right\rangle = 12V^2$, $(1/T_1)_{H||c} \propto Tr \left\langle H_i^{hf} H_j^{hf} \right\rangle - \left\langle H_3^{hf} H_3^{hf} \right\rangle = 8V^2$, the anisotropy ratio is again 1.5, as expected from the fact that the fluctuations have the same wave vector as for the stripe case

Finally, for bi-collinear correlations, $\mathbf{Q} \approx (\pi, \pi)$, the possible patterns are $\begin{pmatrix} + & - \\ + & + \end{pmatrix}$ and three partners obtained by rotating the "−" site. Now

$$T = \begin{pmatrix} 2 & 2 & -2 \\ 2 & 2 & 2 \\ -2 & 2 & 2 \end{pmatrix}, \begin{pmatrix} 2 & 2 & 2 \\ 2 & 2 & -2 \\ 2 & -2 & 2 \end{pmatrix}, \begin{pmatrix} 2 & -2 & 2 \\ -2 & 2 & 2 \\ 2 & 2 & 2 \end{pmatrix}, \begin{pmatrix} 2 & -2 & -2 \\ -2 & 2 & -2 \\ -2 & -2 & 2 \end{pmatrix}, \tag{28}$$

$$\left\langle H_i^{hf} H_j^{hf} \right\rangle = \begin{pmatrix} 4X^2 + o & 0 & 0 \\ 0 & 4X^2 + o & 0 \\ 0 & 0 & 4Z^2 + o \end{pmatrix}. \tag{29}$$

In the last line, o means combinations of the off-diagonal couplings, which are much smaller than the diagonal one. The full calculation renders $(1/T_1)_{H||a} = (1/T_1)_{H||b} \propto 4X^2 + 4Z^2 + 4U^2 + 12V^2$, $(1/T_1)_{H||c} \propto 8X^2 + 8U^2 + 8V^2$, the anisotropy thus is $(X^2 + Z^2 + U^2 + 3V^2)/2(X^2 + U^2 + V^2) \approx (X^2 + Z^2)/2X^2$, and thus depends on the anisotropy of the diagonal hyperfine coupling, which, if the Fermi-contact coupling dominates, is small.

For plaquette correlation, there are four patterns $\begin{pmatrix} + & + \\ + & + \end{pmatrix}$, $\begin{pmatrix} + & + \\ - & - \end{pmatrix}$, $\begin{pmatrix} + & - \\ + & - \end{pmatrix}$, and $\begin{pmatrix} + & - \\ - & + \end{pmatrix}$, which have the same probability. Correspondingly, we have

$$T = \begin{pmatrix} 4 & 0 & 0 \\ 0 & 4 & 0 \\ 0 & 0 & 4 \end{pmatrix}, \begin{pmatrix} 0 & 0 & 4 \\ 0 & 0 & 0 \\ 4 & 0 & 0 \end{pmatrix}, \begin{pmatrix} 0 & 0 & 0 \\ 0 & 0 & 4 \\ 0 & 4 & 0 \end{pmatrix}, \begin{pmatrix} 0 & 4 & 0 \\ 4 & 0 & 0 \\ 0 & 0 & 0 \end{pmatrix}, \tag{30}$$

$$\left\langle H_i^{hf} H_j^{hf} \right\rangle = \frac{1}{4} \left[\begin{pmatrix} 16X^2 & 0 & 0 \\ 0 & 16X^2 & 0 \\ 0 & 0 & 16Z^2 \end{pmatrix} + \begin{pmatrix} 16V^2 & 0 & 0 \\ 0 & 0 & 0 \\ 0 & 0 & 16V^2 \end{pmatrix} + \begin{pmatrix} 0 & 0 & 0 \\ 0 & 16V^2 & 0 \\ 0 & 0 & 16V^2 \end{pmatrix} + \begin{pmatrix} 16U^2 & 0 & 0 \\ 0 & 16U^2 & 0 \\ 0 & 0 & 0 \end{pmatrix} \right] \tag{31}$$

$$= \begin{pmatrix} 4X^2 + o & 0 & 0 \\ 0 & 4X^2 + o & 0 \\ 0 & 0 & 4Z^2 + o \end{pmatrix}. \tag{32}$$

The result reads: $(1/T_1)_{H||a} = (1/T_1)_{H||b} \propto 8X^2 + 8Z^2 + 12V^2, \propto 4X^2 + 4Z^2 + 4U^2 + 12V^2$ $(1/T_1)_{H||c} \propto 16X^2 + 8V^2, \propto 8X^2 + 8U^2 + 8V^2$ the anisotropy thus is $(2X^2 + 2Z^2 + 3V^2)/2(2X^2 + V^2) \approx (X^2 + Z^2)/2X^2, (4X^2 + 4Z^2 + 4U^2 + 12V^2)/(8X^2 + 8U^2 + 8V^2) \approx (X^2 + Z^2)/2X^2$, same as for the bilinear fluctuations.

Supplementary Fig. 8 shows the temperature dependence of the anisotropy ratio $R = T_{1,a}^{-1}/T_{1,c}^{-1}$ in our measurements. The anisotropy at high temperatures is $R \equiv T_{1,a}^{-1}/T_{1,c}^{-1} \approx 1.5$, similar to that found in other iron pnictides [34, 36]. This observation strongly suggest that the $(\pi, 0)$ correlations of isotopic Fe spins are dominating in Sr_2VO_3FeAs at the high temperatures, as in the case of other iron pnictides. However, with lowering temperature, R is strongly enhanced up to $R \sim 6$ near T_0 (presumably, reflecting magnetocrystalline anisotropy that makes the incipient critical temperature be different for different spin directions) before rapidly dropping to $R \sim 1$ below T_0. R remains almost the same with further lowering temperatures, which never recover back to $R \sim 1.5$ near $T_N \approx 45$ K. This result implies that the dominant spin fluctuations in that temperature range are not of stripe-type and herald an onset of
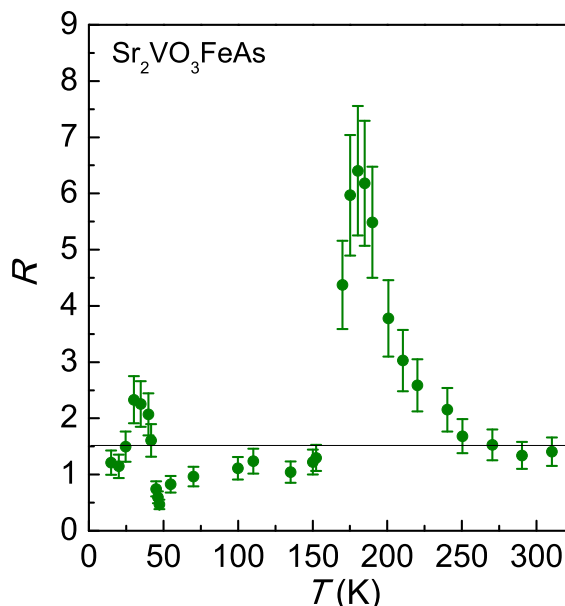

Supplementary Fig. 8: The anisotropy of spin-lattice relaxation rate $R \equiv T_{1,a}^{-1}/T_{1,c}^{-1}$ as a function of temperature. The horizontal line corresponds to the expected value for the stripe AFM correlation.

a spin order with a Q different from $(0, \pi)$. The long-pitch spin density wave with $Q = (1/8, 1/8, 0)$, suggested in the recent neutron powder diffraction [3], is a viable candidate. These results clearly demonstrate that not only the unusual C_4 symmetric transition at T_0, but also the magnetic transition at T_N is highly distinct from those found in other iron pnictides.

Supplementary Note 7. The ordered Fe magnetic moment below $T_N = 45$ K

From the full width at half maximum (FWHM) the As NMR peak ~ 0.5 MHz , as shown in Fig. 2c in the main text, one can roughly estimate the ordered moment of Fe at low temperatures. For the spin density wave phase with $Q = (1/8, 1/8, 0)$, the As environment is spin-imbalanced, and thus the diagonal hyperfine coupling will be dominant. In order to estimate the diagonal Fe-As hyperfine coupling, we have performed WIEN2k calculations keeping the V sublattice in the Mott insulating (antiferromagnetic) state and all Fe equivalent and ferromagnetic. We have performed both GGA and LDA calculations, which allow us to sample more magnetic moments, and also scaled the exchange field with different coefficients as described in Ref. [37]. The calculated hyperfine filed was then rescaled back with the inverse coefficient. In Supplementary Fig. 9 we plotted the average values of hyperfine field at the two inequivalent As sites, which experience induced by V hyperfine fields of the opposite signs. We note that the coupling comes mostly from the Fermi-contact term, the core polarization was taken into account but was smaller.
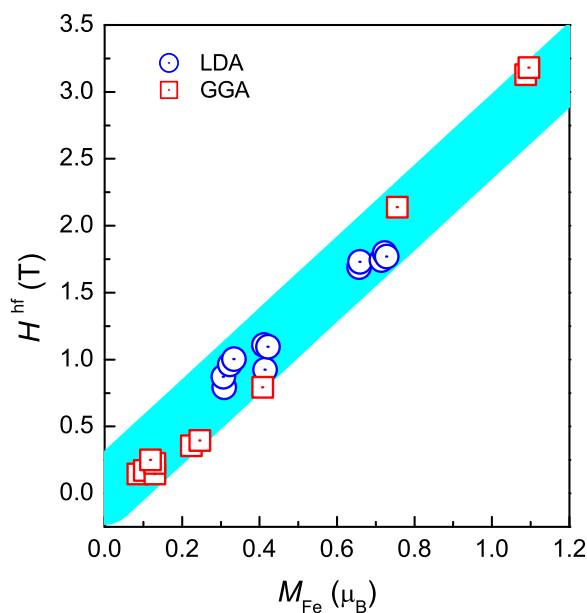
Supplementary Fig. 9: Calculated induced contact hyperfine field on the As site as a function of the net Fe magnetic moment.

The resulting diagonal coupling is $4A_{hf} \approx 2.5$ T/μ_B, which is somewhat larger than the typical off-diagonal hyperfine coupling $4A_{hf} \approx 1.7$ T/μ_B [21]. For a spiral with $Q = (1/8, 1/8, 0)$ we would expect a net polarization around As to be ~ 0.6 M, where M is the Fe moment. Using the nuclear gyromagnetic ratio 7.292 MHz/T for As and $4A_{hf} \approx 2.5$ T/μ_B, the internal field H_{in} of As sites can be estimated to be $H_{in} = 4A_{hf} \times 0.6M_0 \sim 800$ Oe. This corresponds to the upper bound of Fe moments ~ 0.05 μ_B, an order of magnitude smaller than found in other iron pnictides. Such a small Fe moments are also consistent with the estimates from neutron powder diffraction [3] and μSR spectroscopy [31].

In the previous Fe Mössbauer spectroscopy studies on polycrystalline Sr_2VO_3FeAs samples [1, 31], negligible line splitting or broadening was observed, which has been taken as experimental evidence of no static Fe spin ordering. However, the Fe Mössbauer spectra of polycrystalline Sr_2VO_3FeAs samples have a double peak structure and also a large FWHM already at room temperature, which hampers observation of magnetic ordering with such a small Fe moment less than 0.05 μ_B. As shown in the case of the isostructural compound Sr_2ScO_3FeAs, the line broadening of the Fe Mössbauer spectra is not at all obvious when the ordered moments is as small as ~ 0.05 μ_B [31]. In strong contrast, the ^{75}As NMR line broadening observed at high temperature is an order of magnitude smaller than found

below T_N, which allow us to detect the Fe magnetic ordering of Sr_2VO_3FeAs single crystal in our study. From this comparison, one can say that, although it is not direct probe, ^{75}As NMR is much more sensitive to the ordering of small Fe moments in Sr_2VO_3FeAs, than Fe Mössbauer spectroscopy.

---

[1] G. H. Cao *et al.*, "Self-doping effect and successive magnetic transitions in superconducting $Sr_2VFeAsO_3$," Phys. Rev. B **82**, 104518 (2010).

[2] S. Tatematsu *et al.*, "Magnetic ordering in V-layers of the superconducting system of $Sr_2VFeAsO_3$," J. Phys. Soc. Jpn. **79**, 123712 (2010).

[3] M. Tegel *et al.*, "Possible magnetic order and suppression of superconductivity by V doping in Sr_2VO_3FeAs," Phys. Rev. B **82**, 140507 (2010).

[4] S. Kasahara *et al.*, "Electronic nematicity above the structural and superconducting transition in $BaFe_2(As_{1-x}P_x)_2$," Nature **486**, 382 (2012).

[5] M. A. Tanatar *et al.*, "Direct imaging of the structural domains in the iron pnictides AFe_2As_2 (A=Ca,Sr,Ba)," Phys. Rev. B **79**, 180508 (2009).

[6] M. Rotter *et al.*, "Spin-density-wave anomaly at 140 K in the ternary iron arsenide $BaFe_2As_2$," Phys. Rev. B **78**, 020503 (2008).

[7] N. Qureshi *et al.*, "Crystal and magnetic structure of the oxypnictide superconductor $LaFeAsO_{1-x}F_x$: A neutron-diffraction study," Phys. Rev. B **82**, 184521 (2010).

[8] R. Klingeler *et al.*, "Local antiferromagnetic correlations in the iron pnictide superconductors $LaFeAsO_{1-x}F_x$ and $Ca(Fe_{1-x}Co_x)_2As_2$ as seen via normal-state susceptibility," Phys. Rev. B **81**, 024506 (2010).

[9] G. F. Chen *et al.*, "Multiple phase transitions in single-crystalline $Na_{1-\delta}FeAs$," Phys. Rev. Lett. **102**, 227004 (2009).

[10] D. C. Johnston, "The puzzle of high temperature superconductivity in layered iron pnictides and chalcogenides," Advances in Physics **59**, 803 (2010).

[11] L. Y. Xing *et al.*, "Observation of non-Fermi liquid behavior in hole-doped $LiFe_{1-x}V_xAs$," Phys. Rev. B **94**, 094524 (2016).

[12] M. D. Lumsden and A. D. Christianson *et al.* "Magnetism in Fe-based superconductors," J. Phys. Condens. Matter **22**, 203203 (2010).

[13] R. M. Fernandes *et al.*, "What drives nematic order in iron-based superconductors?," Nat. Phys. **10**, 97-104 (2014).

[14] S.-H. Baek *et al.*, "Orbital-driven nematicity in FeSe," Nat. Mater. **14**, 210 (2015).

[15] F. Ma *et al.*, "First-principles calculations of the electronic structure of tetragonal α-FeTe and α-FeSe crystals: evidence for a bicollinear antiferromagnetic order," Phys. Rev. Lett. **102**, 177003 (2009).

[16] S. Avci *et al.*, "Magnetically driven suppression of nematic order in an iron-based superconductor," Nat. Commun. **5**, 3845 (2014).

[17] A. E. Böhmer *et al.*, "Superconductivity-induced re-entrance of the orthorhombic distortion in $Ba_{1-x}K_xFe_2As_2$," Nat. Commun. **6**, 7911 (2015).

[18] J. M. Allred *et al.*, "Double-Q spin-density wave in iron arsenide superconductors," Nat. Phys. **12**, 493 (2016).

[19] F. Waβer *et al.*, "Spin reorientation in $Ba_{0.65}Na_{0.35}Fe_2As_2$ studied by single-crystal neutron diffraction," Phys. Rev. B **91**, 060505 (2015).

[20] K. Kitagawa *et al.*, "Crossover from commensurate to incommensurate antiferromagnetism in stoichiometric NaFeAs revealed by single-crystal $^{23}Na,^{75}As$-NMR experiments," J. Phys. Soc. Jpn. **80**, 033705 (2011).

[21] K. Kitagawa *et al.*, "Commensurate itinerant antiferromagnetism in $BaFe_2As_2$: ^{75}As-NMR studies on a self-flux grown single crystal," J. Phys. Soc. Jpn. **77**, 114709 (2008).

[22] F. L. Ning *et al.*, "Contrasting spin dynamics between underdoped and overdoped $Ba(Fe_{1-x}Co_x)_2As_2$," Phys. Rev. Lett. **104**, 037001 (2010).

[23] K. Kitagawa *et al.* "Antiferromagnetism of $SrFe_2As_2$ studied by single-crystal ^{75}As-NMR," J. Phys. Soc. Jpn. **78**, 063706 (2009).

[24] M. Long *et al.* "Quenched Fe moment in the collapsed tetragonal phase of $Ca_{1-x}Pr_xFe_2As_2$," Chin. Phys. B **22**, 057401 (2013).

[25] Y. Furukawa *et al.*, "Suppression of electron correlations in the collapsed tetragonal phase of $CaFe_2As_2$ under ambient pressure demonstrated by ^{75}As NMR/NQR measurements," Phys. Rev. B **89**, 121109 (2014).

[26] S. Avci *et al.*, "Magnetically driven suppression of nematic order in an iron-based superconductor," Nat. Commun. **10**, 4845 (2013).

[27] Y. Nakai *et al.*, "Evolution from itinerant antiferromagnet to unconventional superconductor with fluorine doping in $LaFeAs(O_{1-x}F_x)$ revealed by ^{75}As and ^{139}La nuclear magnetic resonance," J. Phys. Soc. Jpn. **77**, 073701 (2008).

[28] R. Sakurai *et al.*, "Quantum critical behavior in heavily doped $LaFeAsO_{1-x}H_x$ pnictide superconductors analyzed using nuclear magnetic resonance," Phys. Rev. B **91**, 064509 (2015).

[29] H. Kinouchi *et al.*, "Antiferromagnetic spin fluctuations and unconventional nodeless superconductivity in an iron-based new superconductor $(Ca_4Al_2O_{6-y})(Fe_2As_2)$: ^{75}As nuclear quadrupole resonance study," Phys. Rev. Lett. **107**, 047002 (2011).

[30] K. Yamamoto *et al.*, "Antiferromagnetic order and superconductivity in $Sr_4(Mg_{0.5-x}Ti_{0.5+x})_2O_6Fe_2As_2$ with electron

doing: ^{75}As-NMR study," J. Phys. Soc. Jpn. **81**, 053702 (2012).

[31] J. Munevar *et al.*, "Static magnetic order of $Sr_4A_2O_6Fe_2As_2$ (A = Sc and V) revealed by Mössbauer and muon spin relaxation spectroscopies," Phys. Rev. B **84**, 024527 (2011).

[32] S. Backes *et al.* "Microscopic nature of correlations in multiorbital AFe_2As_2 (A = K, Rb, Cs): Hund's coupling versus Coulomb repulsion," Phys. Rev. B **92**, 195128 (2015).

[33] M. Yi *et al.* "Symmetry-breaking orbital anisotropy observed for detwinned $Ba(Fe_{1-x}Co_x)_2As_2$ above the spin density wave transition," Proc. Natl. Acad. Sci. USA **108**, 6878 (2011).

[34] K. Kitagawa *et al.*, "Stripe antiferromagnetic correlations in $LaFeAsO_{1-x}F_x$ probed by ^{75}As NMR," Phys. Rev. B **81**, 212502 (2010).

[35] M. Hirano *et al.*, "Potential antiferromagnetic fluctuations in hole-doped iron-pnictide superconductor $Ba_{1-x}K_xFe_2As_2$ studied by ^{75}As nuclear magnetic resonancemeasurement," J. Phys. Soc. Jpn. **81**, 054704 (2012).

[36] J. Cui *et al.*, "Antiferromagnetic spin correlations and pseudogaplike behavior in $Ca(Fe_{1-x}Co_x)_2As_2$ studied by ^{75}As nuclear magnetic resonance and anisotropic resistivity," Phys. Rev. B **92**, 184504 (2015).

[37] L. Ortenzi, *et al.*, "Accounting for spin fluctuations beyond local spin density approximation in the density functional theory," Phys. Rev. B **86**, 064437 (2012).